ADVANCING EARTH AND SPACE SCIENCES

JGR Atmospheres

RESEARCH ARTICLE

10.1029/2025JD045547

Key Points:

- Extreme supersaturations up to 11% were estimated from 219 updraft cores with in situ peak updraft measurements reaching 28 m s^{-1}
- Case studies show that high supersaturations are linked to the developing stage and may support condensational invigoration
- Supersaturations exceeding 1% are more probable to occur at subfreezing temperatures and with stronger updrafts

Correspondence to:

S. Patil,
saurabh@ou.edu

Citation:

Patil, S., McFarquhar, G. M., Huang, Y., Roberts, G., Wolde, M., Nichman, L., et al. (2026). Quasi-steady state supersaturation: Do high values derived from ESCAPE represent real high supersaturations and the potential for condensational invigoration? *Journal of Geophysical Research: Atmospheres*, *131*, e2025JD045547. https://doi.org/10.1029/2025JD045547

Received 30 SEP 2025
Accepted 26 MAY 2026

Quasi-Steady State Supersaturation: Do High Values Derived From ESCAPE Represent Real High Supersaturations and the Potential for Condensational Invigoration?

Saurabh Patil[1,2], Greg M. McFarquhar[1,2], Yongjie Huang[1,3], Greg Roberts[4,5], Mengistu Wolde[6], Leonid Nichman[6], Cuong Nguyen[6], Keyvan Ranjbar[6], Natalia Bliankinshtein[6], Amanda Richter[1,2], Pavlos Kollias[7,8], and Daniel Rosenfeld[9]

[1]School of Meteorology, University of Oklahoma, Norman, OK, USA, [2]Cooperative Institute of Severe and High-Impact Weather Research and Operations (CIWRO), Norman, OK, USA, [3]Center for Analysis and Prediction of Storms, University of Oklahoma, Norman, OK, USA, [4]Scripps Institution of Oceanography, University of California San Diego, La Jolla, CA, USA, [5]Centre National de Recherches Météorologiques, Université de Toulouse, Météo-France, CNRS, Toulouse, France, [6]Flight Research Laboratory, National Research Council Canada, Ottawa, ON, Canada, [7]School of Marine and Atmospheric Sciences, Stony Brook University, Stony Brook, NY, USA, [8]Environmental Science and Technologies, Brookhaven National Lab, Upton, NY, USA, [9]Institute of Earth Sciences, The Hebrew University of Jerusalem, Jerusalem, Israel

Abstract Deep convective clouds were intensively sampled during the Experiment of Sea Breeze Convection, Aerosols, Precipitation, and Environment (ESCAPE) with coordinated flights of the NRC Convair-580 and SPEC Learjet. A total of 219 updraft core segments were sampled over coastal Texas and Louisiana under diverse meteorological conditions. Median updraft properties included widths of ∼1 km, velocities of 4.8 m s^{-1}, droplet number concentrations of ∼400 cm^{-3}, and liquid water contents of 0.9 g m^{-3}. The limitations of using the quasi-steady state approximation to derive supersaturations were explored. Supersaturation (S_{QSS}) estimated from in situ observations under a quasi-steady state assumption averaged 0.4% but occasionally exceeded 2%, with values >1% (high supersaturations) identified as statistical outliers. Two case studies illustrated the conditions linked to high supersaturations. In a storm over the Gulf, median core S_{QSS} reached 2.46% in the developing stage compared to 2.17% in the mature stage under similar thermodynamic conditions. In a storm over coastal Louisiana, S_{QSS} peaked near 11% within a 13.7-m s^{-1} updraft, accompanied by predominantly supercooled liquid droplets at −13°C and exceptionally low diameter concentrations of 0.29 mm cm^{-3}. Bootstrap analysis of all sampled cores showed that high supersaturations are most probable in cold and mixed-phase regimes with moderate to strong updrafts and are strongly influenced by vertical velocity and droplet number concentrations. While extreme supersaturations (∼10%) were rare, their occurrence underscores the need for targeted multiplatform observations to resolve their spatiotemporal variability and assess their potential role in deep convective invigoration.

Plain Language Summary Scientists studied thunderstorms along the Texas and Louisiana coasts using research aircraft. They found that most of the rising air currents, or updrafts, were about a kilometer wide and carried large amounts of water upward at average speeds near 5 m per second. Most updrafts showed only slightly higher humidity than saturation, known as supersaturation, but a few cases revealed much higher excesses. In one Gulf storm, a developing cell contained higher supersaturation than a nearby mature cell. In a Louisiana storm, supersaturation briefly reached 11 percent within a strong updraft, allowing liquid water to persist at very low temperatures. Although rare, these brief but extreme conditions may play an important role in storm intensification in polluted environments. Because they are short-lived and difficult to measure, more coordinated aircraft and instrument observations are needed to better understand their impact on extreme weather.

1. Introduction

Deep convective clouds govern the global water cycle and drive hazardous weather such as damaging winds, hail, lightning, and flash floods. Because updraft strength dictates the life cycle of clouds and associated hazards, understanding how aerosols and the environment modulate vertical velocity remains a central challenge (Fan et al., 2025; Grabowski & Morrison, 2020; Koren et al., 2010; Lebo, 2018; Varble, 2018). In turn, the vertical velocity has a big impact on determining cloud microphysical properties (e.g., Huang et al., 2025). Cloud properties are sensitive not only to vertical velocity and other meteorological conditions but also to aerosol amount and composition. One prominent uncertainty in aerosol-cloud-meteorological interactions is the extent to which the warm phase or condensational invigoration hypothesis influences cloud development (Cotton & Walko, 2021; Fan et al., 2018, 2025; Ilan Koren et al., 2014; Sheffield et al., 2015). According to this hypothesis, cloud droplet nucleation, or condensation of water vapor, of additional aerosols in polluted clouds releases more latent heat that enhances the strength of updrafts compared to those in clean clouds. Romps et al. (2023) investigated shallow clouds over the Amazon using the buoyancy drag balance framework to estimate that supersaturations well exceeding 1% are necessary in clean conditions to make substantial warm phase invigoration plausible in polluted conditions. Using the same framework, Fan et al. (2025) found that with a 6% supersaturation, the updraft can increase by up to 8 m s^{-1} for 8 km deep convective mixed-phase clouds. The condensational invigoration is anticipated to have more substantial effects in the future due to a global warming trend in the lower troposphere (Igel & van den Heever, 2021).

Water vapor supersaturation is the amount the actual vapor pressure exceeds its temperature-dependent saturation value. Measuring supersaturation in clouds is currently not possible because it requires highly accurate, unbiased localized measurements of water vapor pressure and temperature, yet liquid droplets, cloud turbulence, the extreme sensitivity of supersaturation to these variables, and the limited response time of instruments constrain measurement accuracy to only a few percent (Ditas et al., 2012; Fujiwara et al., 2003; Korolev & Mazin, 2003; Romps, 2025; Shen et al., 2018; Yeom et al., 2019). Hence, most prior studies have inferred supersaturation indirectly (e.g., Varble et al., 2023) using the quasi-steady state approximation originally proposed by Squires (1952), who suggested that supersaturation in a vertically moving cloud parcel is directly proportional to vertical velocity and inversely proportional to the number concentration and mean size of cloud droplets. Many studies including Warner (1968), Paluch and Knight (1984), Austin et al. (1985), and Politovich and Cooper (1988) used this relationship to derive low mean supersaturations in convective clouds of about 0.2%. However, Prabha et al. (2011) derived supersaturations as high as 5%–8% in central India when boundary layer aerosol concentrations were more than 1,000 cm^{-3}, attributing this to cloud droplet size distribution broadening through in-cloud nucleation in updrafts. All these results were obtained in continental regions where background aerosol concentrations are much larger compared to marine regions. Real-case modeling (Fan et al., 2018) suggested that pristine deep convective clouds can exhibit extreme supersaturation levels (>10%) due to low condensation efficiency as efficient collision-coalescence depletes droplets quickly. However, ultrafine aerosols substantially reduce the supersaturation to 2%–3% due to increased droplet surface area and condensation efficiency. Romps (2025) estimated higher supersaturations in pristine conditions compared to polluted conditions using observations from shallow warm convective clouds. The study reported a median (mean) supersaturation of 0.46% (0.5%) in 41.5 s of updraft measurements during the Amazon rainy season, when mean aerosol concentrations were 328 cm^{-3}, compared to median (mean) supersaturation of 0.13% (0.15%) in 87.5 s of updrafts during the dry season, when mean aerosol concentrations were 1,159 cm^{-3} (Romps et al., 2023). However, the maximum supersaturation computed by Romps (2025) did not exceed 1%. A recent study (Fan et al., 2025) presented high supersaturation estimations from the developing stage of deep convective clouds sampled during Cloud Aerosol Interaction and Precipitation Enhancement Experiment (CAIPEEX IV). Of the 867 1-Hz samples collected during 19 cloud passes from three flights, 3% had quasi-steady state supersaturations exceeding 5% and the maximum supersaturation was 16.7%. However, because the sampled clouds formed under intermediate aerosol conditions with maximum droplet number concentrations of ~600 cm^{-3} at the cloud base, further observational evidence of high supersaturations (>1%) in deep convective clouds in pristine aerosol conditions is still lacking. Such evidence is crucial to support the condensational invigoration hypothesis.

The scarcity of in situ observations under unique conditions potentially conducive to high supersaturations is partly attributed to measurement challenges. Convective clouds evolve rapidly, with properties that vary in space and time, while higher supersaturations might be expected during their developing stages. However, prior airborne observational studies of the invigoration hypothesis were unable to provide a comprehensive description of the spatiotemporal context of reported microphysical properties, including supersaturations (Varble et al., 2023). Another limitation of previous studies is the restriction of analysis to regions with in-cloud temperatures near 0°C. However, exceptionally strong updrafts can locally elevate the warm phase (primarily supercooled liquid water) to temperatures as low as −12 to −13°C, where warm phase condensation would still dominate the droplet growth process. Including analysis of supersaturation at such low temperatures in liquid-phase conditions is crucial for testing the invigoration hypothesis, as modeling studies suggest higher supersaturations are anticipated at higher altitudes exceeding 4 km (Fan et al., 2018). More observations at these low temperatures are critically needed.

To isolate the effects of aerosols and meteorology on clouds and precipitation in developing convection, the Experiment of Sea-breeze, Convection, Aerosols, Precipitation and Environment (ESCAPE) campaign was conducted in the vicinity of Houston, Texas, from 30 May to 30 September 2022 (Dzambo et al., 2025; Jensen et al., 2025; Kollias et al., 2025). The National Research Council Canada (NRC) Convair-580 aircraft (NRC, 2025), equipped with aerosol, cloud microphysics, and remote sensing instruments, conducted a total of 13 research flights (CRF). Additionally, the Stratton Park Engineering Company (SPEC) Learjet aircraft, equipped with cloud microphysical and remote sensing instruments, flew 11 research flights (LRF). Except for CRF09 and CRF10, which focused on characterizing the aerosol heterogeneity near Houston (Patnaude et al., 2025; Roberts et al., 2026), all flights concentrated on sampling convective clouds. The research flights were conducted between 30 May and 17 June 2022. A unique aspect of ESCAPE is the extensive sampling of cloud and thermodynamic observations in intense updrafts, reaching velocities up to 28 m s^{-1}, conditions where high supersaturations are hypothesized to occur. Further, observations were collected in pristine clouds over the Gulf south of Houston, continental clouds west of Houston, and polluted clouds east of Houston. This study leverages in situ measurements in powerful updrafts at elevated altitudes in diverse aerosol background conditions collected during ESCAPE to quantify supersaturations. The study capitalizes on the synergy between airborne in situ probes, airborne radars and ground-based Next Generation Weather Radar (NEXRAD) observations to provide the spatial and temporal context necessary for understanding where supersaturation estimates were within convective clouds.

The remainder of the paper is organized as follows. Section 2 presents the value-added cloud microphysics data product developed from the ESCAPE data, which uses machine learning algorithms to improve the quality of the cloud microphysical properties data sets. Section 3 outlines the methodology employed to define convective updraft cores and estimate quasi-steady state supersaturations. Section 4 provides both comprehensive and vertical statistics of microphysical properties and derived supersaturations in sampled updraft cores. Case studies of high supersaturation instances from the SPEC Learjet and NRC Convair-580 aircraft platforms are discussed, followed by the probability of occurrence of high supersaturation values. Section 5 interprets the results and contextualizes them within the current understanding of the condensational invigoration mechanism. While acknowledging the caveats and limitations of the employed methods, Section 6 highlights the key findings.

2. Data and Quality Control

2.1. Deriving Microphysical Parameters

Data from the cloud scattering probes, on the NRC Convair-580, were processed to determine the cloud droplet number distribution function $N(D)$ at 1-Hz resolution and sorted into bins of varying widths. From the derived $N(D)$, bulk microphysical properties such as the total number concentration (N), liquid water content (LWC), and mean diameter (D_{mean}) were calculated using

$$N = \sum_{i=1}^{k} N_i \Delta D_i \tag{1}$$

$$\text{LWC} = \frac{\pi \rho}{6} \sum_{i=1}^{k} N_i \, D_i^3 \, \Delta D_i \tag{2}$$

$$D_{\text{mean}} = \frac{1}{\text{N}} \sum_{i=1}^{k} N_i \, D_i \, \Delta D_i \tag{3}$$

where D_i is the representative diameter of bin i, ΔD_i is the width of bin i, N_i is the number distribution function per bin i, k is the total number of size bins, and r is the density of liquid water. Data from the cloud scattering probes on the SPEC Learjet were processed, and bulk parameters were also calculated using Equations 1–3. Hereafter, the subscript following a microphysical variable represents the probe used to derive that variable (e.g., N_{CDP}

represents total number concentrations derived using specified bins from the cloud droplet probe (CDP)). Further note that symbols $N_{<50}$ and those without an instrument name as subscript (e.g., LWC, D_{mean}) denotes microphysical properties for cloud droplets' size range here assumed to be 3–50 μm.

The Optical Array Probe (OAP) data from both the NRC Convair-580 and SPEC Learjet were processed using the University of Illinois/Oklahoma Optical Array Probe Software (UIOOPS, McFarquhar et al., 2018) to determine $N(D)$ at a frequency of 1-Hz and to provide particle images. Two OAPs, namely the 2-Dimentional Stereo (2DS) probe and High-Volume Precipitation Spectrometer version 3 (HVPS-3), nominally measure hydrometeors in the size range of 10–1,280 μm and 150–19,200 μm, respectively. However, the derived $N(D)$ is highly uncertain at the smallest sizes due to a poorly defined depth of field for smaller particles. The depth of field is proportional to the size squared of the particle and therefore is small for small particles when their shadow is only a small number of pixels. This uncertainty is propagated into the calculation of sample volume per unit time, which is required to derive the final $N(D)$. Since the CDP can measure sizes up to 50 μm and 2DS up to 1,280 μm, the 2DS and HVPS-3 bin sizes were carefully selected from 45 to 1,305 μm and 1,275 to 6,375 μm, respectively, in order to minimize uncertainty in the depth of field and to maintain consistent overlap across bin range. The 2DS instrument has horizontal (H) and vertical (V) independent channels that are spatially perpendicular to one another. With an ideal alignment between the two arms, spherical particles entering the probe's sample volume should be detected on both channels in a manner that is similar. However, maintaining such alignment is challenging in the presence of strong updrafts, necessitating the consideration of one of the two channels for the derivation of microphysical variables. Figure 1 shows that the correlation between the total number concentration N and LWC derived from the H and V channels of the 2DS is statistically significant with a Spearman correlation coefficient of at least 0.97. This indicates that either H or V or an average of H and V channels can be used for $N(D)$. However, the V channel was used because the H channel was diagnosed with a consistent dead diode on the SPEC Learjet flights, even though it did not have any significant impact on the derived size distributions. Note that the LWC derived for the correlation purpose from the 2DS probe assumed a spherical shape of the particles independent of their phases. Further detailed information regarding microphysical measurement uncertainties is discussed in Baumgardner et al. (2017) and McFarquhar et al. (2017).

2.2. Time and Baseline Offset Corrections Using Data Driven Methods

The cloud probes on the NRC Convair-580 were operated with several independent acquisition systems. Thus, if the probe clocks were not properly initialized before a flight, there could be an offset between times meaning that one probe could be lagging or leading another probe. This can be especially problematic when examining the properties of developing cumuli, which typically have narrow spatial cross-section scales and are horizontally inhomogeneous. The time offsets between cloud probes were determined by comparing the time series of LWC measured by the Nevzorov probe ($\mathrm{LWC}_{\mathrm{Nevzorov}}$), CDP ($\mathrm{LWC}_{\mathrm{CDP}}$), and FCDP ($\mathrm{LWC}_{\mathrm{FCDP}}$). The normalized full linear cross-correlation method (Proakis & Manolakis, 2021) was implemented using the Python NumPy library (Harris et al., 2020) to find the best estimate of the time lag between the cloud probes. Further, to reduce the noise in the correlation signal originating from low-frequency (1-Hz) measurements, a Gaussian filtering algorithm (Virtanen et al., 2020) was applied to these cross-correlation results to identify a distinct lag value. A cross-correlation of 1 at lag 0 means that the time series of the cloud probes being compared are perfectly correlated and synchronous with each other.

Figure 2a shows an example of the cross-correlation analysis for CRF01 on 31 May 2022. The green line, which shows cross-correlation values obtained at lags ranging from −10 to 10 s, is at maximum for a lag of −1 s, giving the optimal offset to align the second time series (here $\mathrm{LWC}_{\mathrm{CDP}}$) with respect to the first (here $\mathrm{LWC}_{\mathrm{Nevzorov}}$). The red dashed line that shows the same cross-correlations with the applied Gaussian smoothing is also at maximum at −1 s, which hence represents the optimum offset for this case. Similar methodology was applied to all cases and Table 1 shows a list of time offsets between instruments found for all NRC Convair-580 research flights using the optimal lag indicated by the Gaussian smoothing curves.

The time offsets listed in Table 1 were added to each respective time series as a final time offset adjustment. Figure 2b shows the time series before and after the time offset adjustment from a 1-min flight segment (15:33:30–15:34:30 UTC) from CRF01 on 31 May 2022. Here, the peak values of $\mathrm{LWC}_{\mathrm{CDP}}$ after the offset adjustment (green line) are seen to better align with $\mathrm{LWC}_{\mathrm{Nevzorov}}$ (red dashed line) compared to the original $\mathrm{LWC}_{\mathrm{CDP}}$ before time offset adjustment (purple line). After aligning the CDP/FCDP with the Nevzorov probe, the

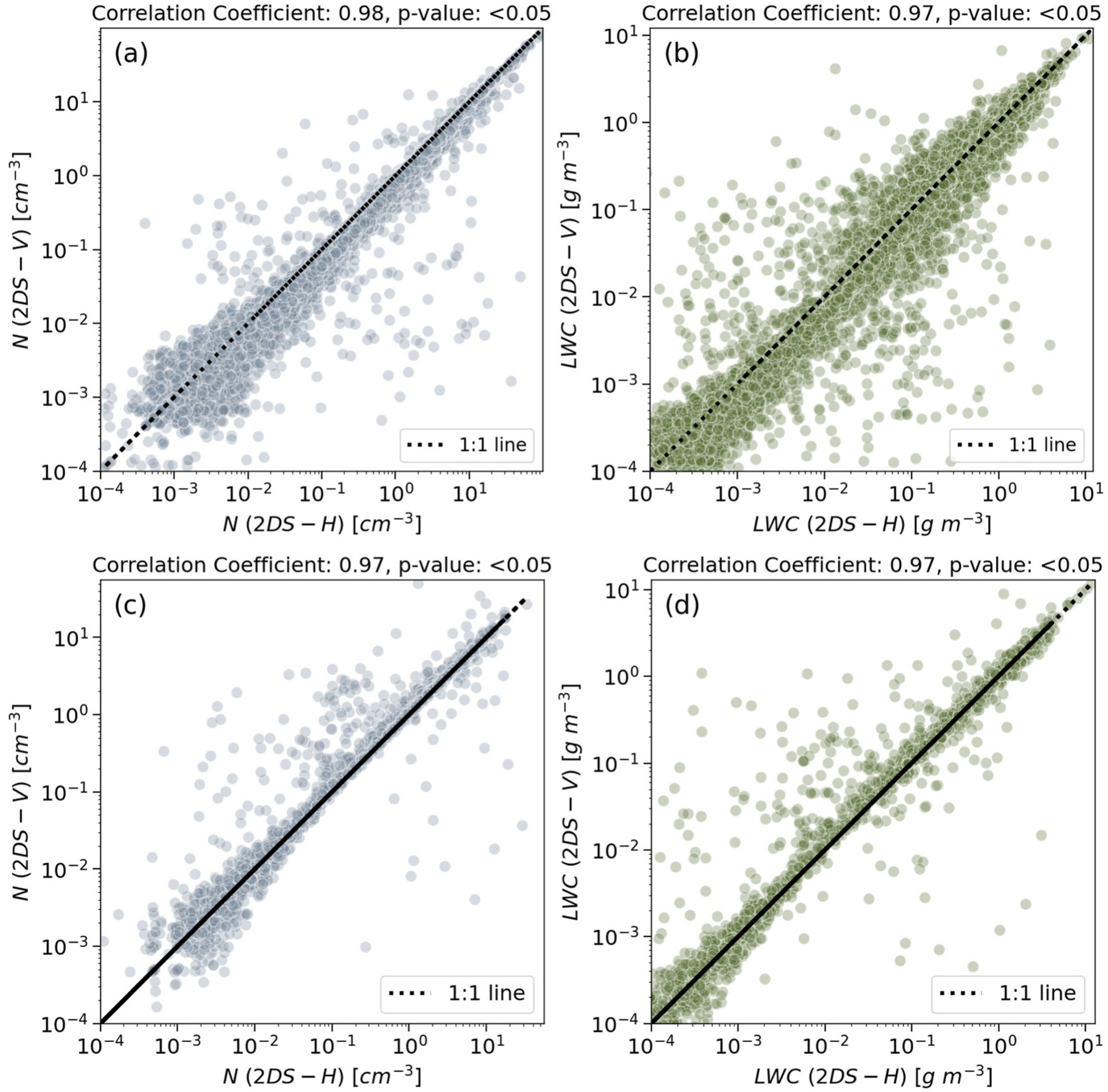

Figure 1. (a) Total cloud droplet number concentration of 2DS for 45 μm < *D* < 1,305 μm in *V* channel as a function of same from the *H* channel measured by the probe installed on NRC Convair-580, having a statistically significant Spearman correlation of 0.98; (b) LWC derived from 2DS V channel size distributions for 45 μm < *D* < 1,305 μm as a function of same from H channel for NRC Convair-580 with statistically significant Spearman correlation of 0.97; (c, d) comparison of *N* and LWC from SPEC Learjet with statistically significant Spearman correlation of 0.97 and 0.97, respectively. Each point in all four subplots represents a 1s average.

2DS probe was aligned with respect to the corrected CDP time series. The time offset between the 2DS probe and CDP was calculated using the LWC derived from the 2DS (LWC_{2DS}) for size bins with *D* between 5 and 65 μm and the LWC_{CDP} derived from 10 to 50 μm bins. To align the HVPS3 with the 2DS, the LWC_{2DS} for particles with 0.2 mm < *D* < 1.2 mm was compared with the LWC derived from the HVPS3 probe (LWC_{HVPS3}) over the same size range. Note that the magnitude of LWC_{2DS} and LWC_{HVPS3} estimates derived using smaller size bins is highly uncertain because of the uncertainty in the depth of field of the instruments, but it does provide information on where 2DS and HVPS3 are detecting small particles and thus can be used to determine an offset. In summary, all probes were manually synchronized for each NRC Convair-580 research flight. No such synchronization efforts were made for the probes installed on the SPEC Learjet as the data were collected on a single data acquisition system simultaneously.

Hot wire probes, such as the Nevzorov LWC sensor, sometimes exhibit a baseline offset due to dynamic heating of the wire. The baseline can drift during the flight as it depends on factors such as the velocity of air surrounding

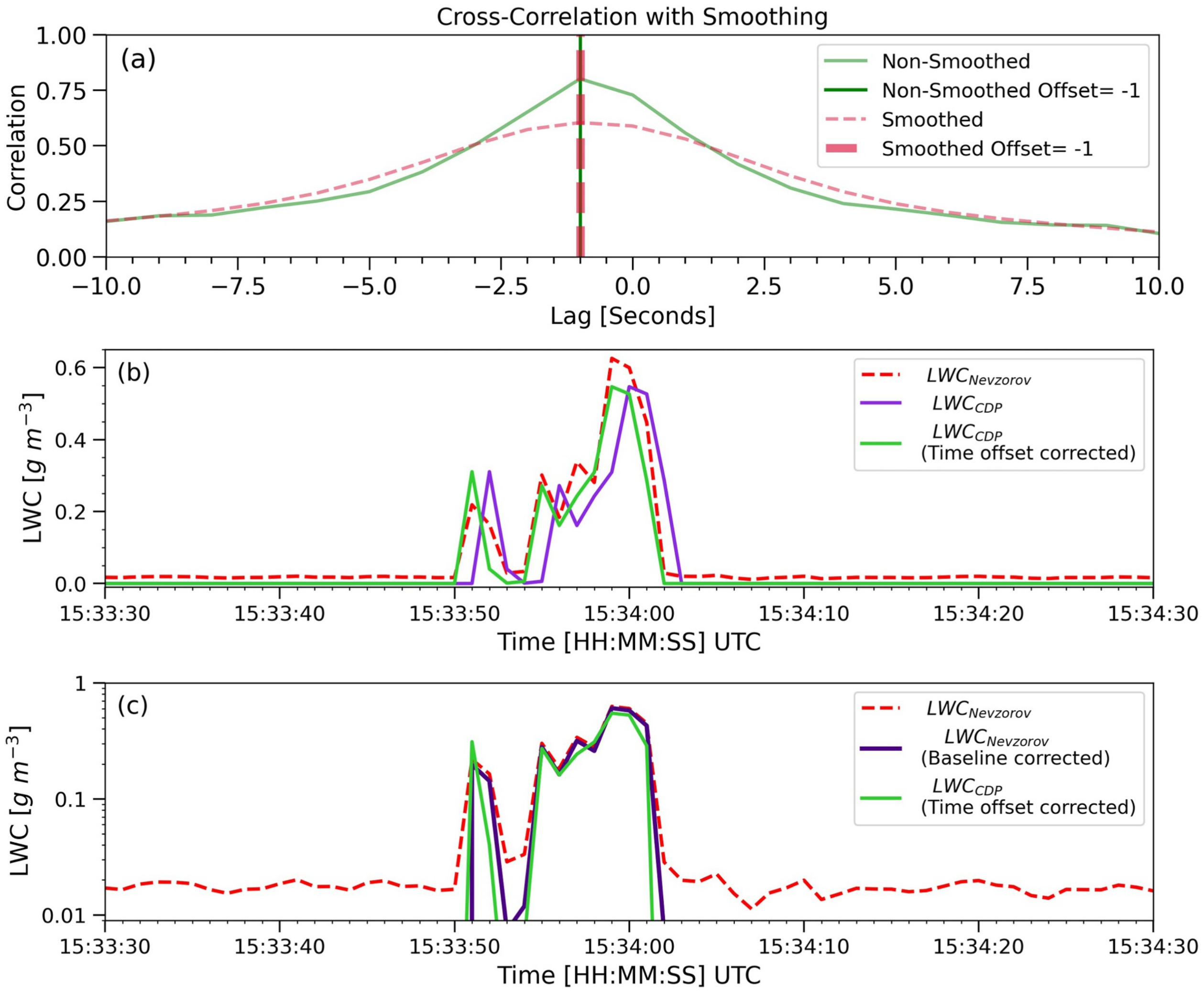

Figure 2. For data acquired during CRF01 on 31 May 2022, (a) dashed red (solid green) line shows cross-correlation with (without) Gaussian smoothing obtained by comparing $\mathrm{LWC_{CDP}}$ timeseries with $\mathrm{LWC_{Nevzorov}}$ time series for lags between −10 and 10 s; vertical dashed red (solid green) line shows optimal time lag corresponding to maximum cross-correlation with (without) Gaussian smoothing. (b) Shows time series between 15:33:30 UTC to 15:34:30 UTC of time offset corrected $\mathrm{LWC_{CDP}}$ (solid green line), $\mathrm{LWC_{Nevzorov}}$ (dashed red line) and non-corrected $\mathrm{LWC_{CDP}}$ (solid purple line); (c) time series of $\mathrm{LWC_{Nevzorov}}$ before baseline offset correction (dashed red line), $\mathrm{LWC_{Nevzorov}}$ after baseline offset correction (solid navy line) and with time offset corrected $\mathrm{LWC_{DP}}$ (solid green line).

the sensor and environmental conditions such as the temperature and relative humidity (Korolev et al., 1998). To correct for its baseline drift, the LWC and total water content (TWC) measured by the Nevzorov probe from all NRC Convair-580 flights were first normalized to a common range of [0, 1] using min-max scaling from the Python Scikit-learn module (Pedregosa et al., 2011). Normalization of the combined data from all flights removes bias due to extreme LWC and TWC and makes clustering analysis more reliable. The K-means algorithm then used the normalized data to identify two clusters, one representing measurement outside clouds and the other representing in-cloud measurements. The smaller cluster center representing baseline noise outside the cloud was then inversely transformed to the original scale to be subtracted from all datapoints to correct the measurements. Slightly negative values (up to $-0.15\ \mathrm{g\ m^{-3}}$ for LWC and $-0.09\ \mathrm{g\ m^{-3}}$ for TWC) resulting from the adjustment were set to zero, as negative LWC and TWC are not physically meaningful. Figure 2c shows an example of the measured Nevzorov LWC before and after the baseline corrections were applied. For the given period, the uncorrected data have an average $\mathrm{LWC_{Nevzorov}}$ of $0.018\ \mathrm{g\ m^{-3}}$ for periods outside the cloud, which are defined here to be time periods with $\mathrm{LWC_{CDP}} < 0.01\ \mathrm{g\ m^{-3}}$ following McFarquhar and Heymsfield (2001). After the baseline correction, the average $\mathrm{LWC_{Nevzorov}}$ is $0.00053\ \mathrm{g\ m^{-3}}$ showing that these periods would not be identified as clouds. For SPEC Learjet, only LRF05 was noted with $\mathrm{LWC_{Nevzorov}}$ below the in-cloud threshold and therefore

Table 1
Time Offsets for Each Instrument During All ESCAPE Flights

	Time offsets relative to nevzorov probe [seconds]				
Research flights	CDP	FCDP	2DS-H	2DS-V	HVPS3
CRF01	−1	0	−2	−2	−48
CRF02	−2	−1	−3	−4	−48
CRF03	−1	0	−1	−1	−46
CRF04	−1	1	−2	−2	−3
CRF05	0	1	0	0	0
CRF06	0	1	0	0	−2
CRF07	−1	1	−1	−1	−3
CRF08	−1	1	−1	−1	−1
CRF11	−1	0	−1	−1	−2
CRF12	0	2	0	0	−1
CRF13	−1	1	−1	−1	−1

Note. Values are unique to each instrument for each flight. Negative values mean the instruments behind Nevzorov probe, and positive means the instrument leads Nevzorov probe. Offset values in unit of s.

was corrected using the K-means algorithm. The algorithm was not applied to the rest of the flights as no values were found below 0.01 g m^{-3} threshold and therefore were assumed to be already baseline corrected.

2.3. Mass Closure Test for Particles With $D < 50$ μm

Mass closure tests, where the mass derived from size distributions is compared against values measured by the bulk probes, are used to test the consistency of data from different probes. These tests can also be leveraged to choose one forward scattering probe to define $N(D)$ for $D < 50$ μm from each aircraft platform. Figure 3 shows the LWC derived from the $N(D)$ measured by different forward scattering probes on each aircraft as a function of the baseline corrected LWC$_{\text{Nevzorov}}$, with each data point representing 1 Hz observations. However, 10-s rolling averages are considered for investigating the agreement between instruments. Using a larger time window for averaging reduces biases in sampling heterogeneous cumulus clouds resulting from the different time responses and sample volumes due to mounting locations. After comparing 10-s averages for probes on the NRC Convair-580, the median difference between LWC$_{\text{CDP}}$ and LWC$_{\text{Nevzorov}}$ was significantly lower at 19.89% compared to that between LWC$_{\text{FCDP}}$ and LWC$_{\text{Nevzorov}}$ at 76.97%. Therefore, CDP observations were preferred over those from the FCDP from the NRC Convair-580 platform. A slightly higher median difference between LWC$_{\text{CDP}}$ and LWC$_{\text{Nevzorov}}$ (19.89%) than the typical accuracy of the LWC$_{\text{Nevzorov}}$ (10%–15%) (Korolev et al., 1998) is likely due to the inclusion of extreme conditions such as strong updraft periods. After considering time periods with vertical velocities within ±1 m s^{-1}, the median difference is only 16%, which indicates that both CDP and Nevzorov observations agree within their uncertainty range. Figures 3c and 3d use SPEC Learjet observations to compare LWC measured by the Nevzorov probe to LWC derived from $N(D)$ using the Hawkeye-FCDP and the FCDP. After comparing 10 s averages, the median difference between LWC$_{\text{Hawkeye-FCDP}}$ and LWC$_{\text{Nevzorov}}$ was 47.6% and between LWC$_{\text{FCDP}}$ and LWC$_{\text{Nevzorov}}$ was only 10.7%. Hence, FCDP observations from the SPEC Learjet platform were preferred to characterize particles with $D < 50$ μm.

3. Method

3.1. Defining Updraft Core Segments

NRC Convair-580 (SPEC Learjet) is defined to be in cloud when both LWC$_{\text{Nevzorov}} > 0.01$ g m^{-3} and LWC$_{\text{CDP}}$ (LWC$_{\text{FCDP}}$) > 0.01 g m^{-3}. Although LWC derived from the FCDP and CDP are used to characterize the cloud properties, the Nevzorov, FCDP and CDP must exceed the 0.01 g m^{-3} threshold such that tenuous clouds or parts of them are not included.

Updraft cores were previously defined by LeMone and Zipser (1980), Jorgensen et al. (1985), Lucas et al. (1994), and Mascio et al. (2020) as locations where vertical velocities are greater than 1 m s^{-1} for at least 500 m in cloud. Similarly, an updraft core is defined here as any continuous period where vertical velocities greater than 1 m s^{-1} persist for at least 5 s, corresponding to ∼500 m considering a mean true air speed (TAS) of nearly 100 m s^{-1}. The intercepted length of any updraft core segment is the product of the mean TAS during the transect and its total duration. The use of this definition includes 28 updraft core segments with an intercepted length of less than 500 m owing to slower mean TAS in these segments, with the shortest being 415 m. In total, 219 updraft core segments were identified, corresponding to a combined 2,327 s (about 78 min) of observations using data from both aircraft. The NRC Convair-580 sampled 174 (1,878 s) and the SPEC Learjet sampled 45 (449 s) updraft core segments. As shown in Figure 4, the geographical distribution of these updraft cores is scattered from over the ocean to deep inland and from west of Houston Texas to east of Lafayette Louisiana thereby covering urban, suburban, and rural areas along the coast, which is representative of various aerosol backgrounds. In addition, these updraft cores represent different meteorological forcings, such as onshore/offshore flows, surface fronts, and propagating outflow boundaries from mesoscale convective systems.

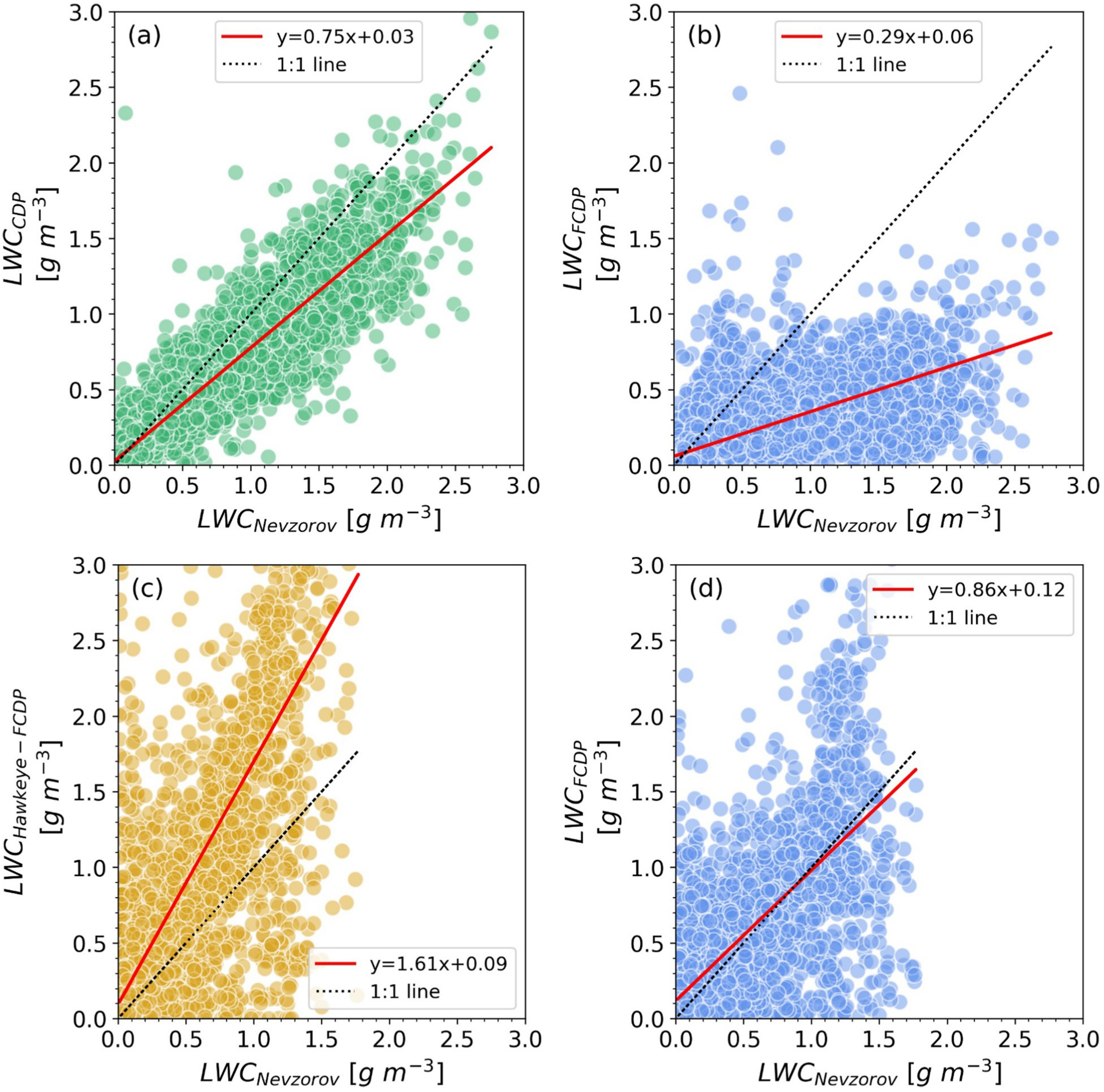

Figure 3. (a) LWC derived from CDP size distributions as a function of baseline corrected LWC from the Nevzorov probe based on NRC Convair-580 observations. (Coefficient of determination, $r^2 = 0.81$) (b) LWC derived from FCDP size distributions as a function of baseline corrected Nevzorov LWC based on NRC Convair-580 observations ($r^2 = 0.48$). (c) LWC derived from Hawkeye-FCDP size distributions as a function of Nevzorov LWC based on SPEC Learjet observations ($r^2 = 0.48$). (d) LWC derived from FCDP size distributions as a function of Nevzorov LWC based on SPEC Learjet observations ($r^2 = 0.40$). Each point represents a 1-Hz observation. The black dotted line is 1:1 line and the red solid line is the best linear fit. Note that extreme values are not shown in the figures for better visual but were included for the median difference estimation.

3.2. Quasi Steady State Supersaturations (S_{QSS})

Direct measurements of supersaturation required to evaluate the invigoration hypothesis are currently not technologically possible due to lack of sufficient accuracy in measuring temperature and humidity in flight (Romps et al., 2023). Hence the supersaturation within updraft cores is estimated using the quasi-steady state approximation (hereafter referred to as quasi-steady supersaturation S_{QSS}) assuming that the portion of the cloud for which S_{QSS} is calculated adiabatically such that there is no transfer of heat or matter with the environment (Squires, 1952). S_{QSS} can be derived using airborne observations of updraft velocity, droplet size distributions, pressure and temperature following Romps et al. (2023) as

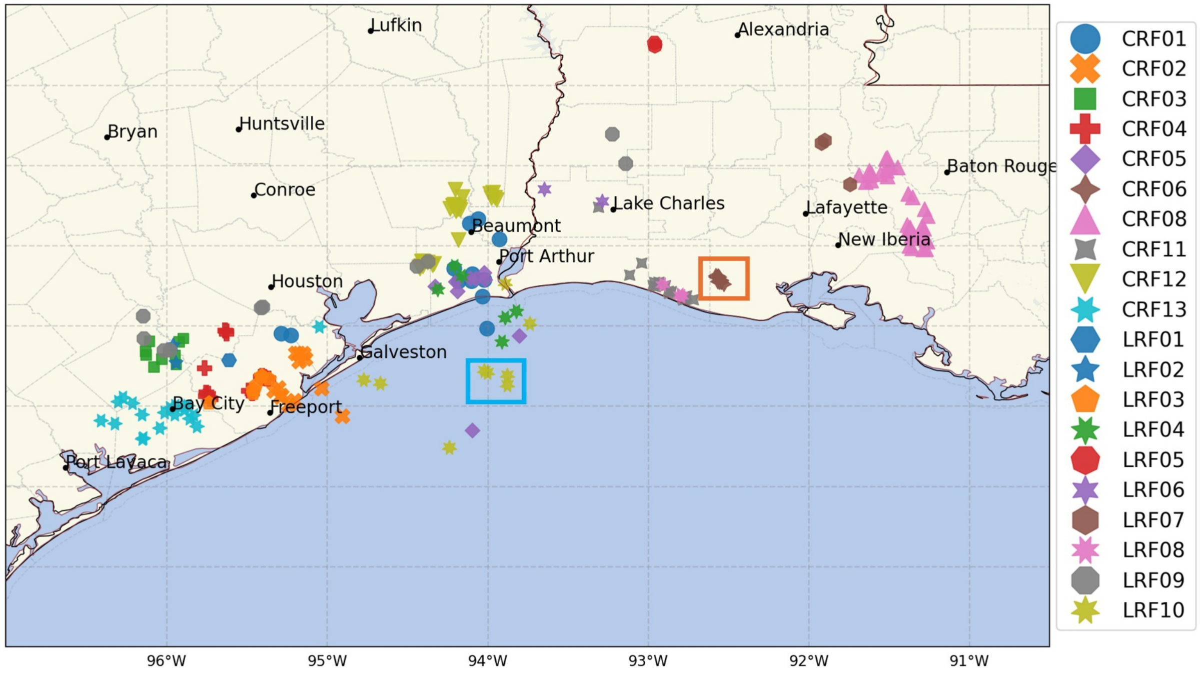

Figure 4. Geographical locations of updraft cores sampled during ESCAPE, with shape and color indicating research flight. Blue and red boxes outline locations of sampled updraft cores described later as high supersaturation cases. Since CRF09 and CRF10 were explicitly dedicated for aerosol observations, no updraft cores were sampled during those flights.

$$S_{\mathrm{QSS}} = \frac{w}{N_{<50}\, D_{\mathrm{mean}}} \frac{g}{2\pi R_a T}\left[\frac{1}{k_d} + \left(\frac{L}{R_v T} - 1\right)\frac{L p_v^*}{R_v T^2}\frac{1}{k_c}\right]\left(\frac{L R_a}{R_v T} - c_p\right)\left(c_p + \frac{R_a L^2 p_v^*}{R_v^2 T^2 p}\right)^{-1} \tag{4}$$

where w is the updraft velocity, $N_{<50}$ is number concentration from 3 μm < D < 50 μm, D_{mean} is the mean diameter of cloud droplets, T is temperature, and p is the air pressure measured using airborne instruments. Other variables such as thermal conductivity of air (k_d), coefficient of diffusion for water vapor in air (k_c), and saturation vapor pressure over liquid (P_v^*) are calculated considering in situ observations of temperature and pressure. The rest of the constants in the equation such as latent heat of vaporization (L), specific gas constant for dry air (R_a), specific gas constant for water vapor (R_v) and specific heat of dry air at constant pressure (C_p) are adapted from Romps (2017) and Romps et al. (2023).

While the quasi-steady state approximation assumes adiabaticity, actual clouds are not adiabatic due to diabatic heating resulting from microphysical processes, radiative heat transfer and continuous mixing with the ambient environment. Although it is difficult to remove the impact of diabatic heating, the latter two uncertainties are minimized by discarding S_{QSS} estimates near cloud boundaries, as they are likely influenced by interactions between cloudy and environmental air. Multiple radiosondes were released from the mobile platforms during the research flights. The cloud base height was estimated as the lifting condensation level (LCL) derived from the closest sounding to the aircraft location. A 1-Hz estimate of S_{QSS} was considered valid when the aircraft was at least 100 m above the cloud base and when there is no cloud-free period (i.e., LWC < 0.01 g m^{-3} from FCDP/CDP and Nevzorov probe) in the 1 s immediately before and after the point S_{QSS} is estimated to ensure the point is at least 100 m distance from the updraft core edges. Furthermore, fixed reflectivity thresholds of 14 dBZ for X-band airborne radar from the NRC Convair-580 and 0 dBZ for Ka-band radar from the SPEC Learjet are used to identify cloud/precipitation edge in the zenith direction to minimize the effects of dry air entrainment from cloud top. The S_{QSS} estimates are only used if they are at least 200 m away from the cloud/precipitation edge detected in the zenith direction. Applying these thresholds to remove data outside clouds or near edges resulted in a total of 1,886 1 Hz S_{QSS} samples from 219 updraft core segments.

Figure 5a shows that the high S_{QSS} occur over a wide range of updraft magnitudes from 5 to 28 m s^{-1} and are particularly pervasive for extremely small diameter concentrations (product of N and D_{mean}; term adapted from

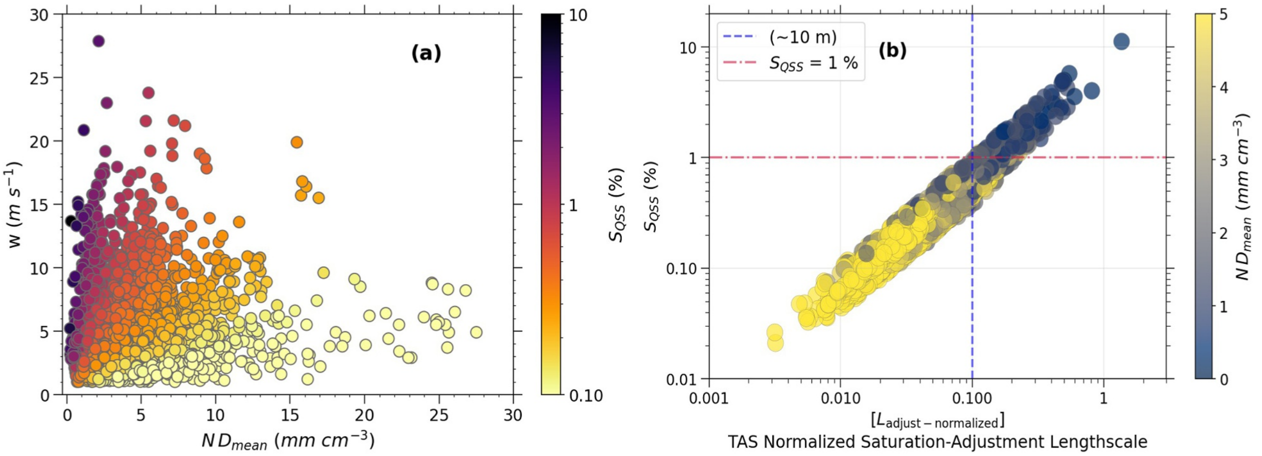

Figure 5. (a) S_{QSS} (colored as a %) derived by using 1-Hz *in situ* measurements of w, N, and D_{mean} in Equation 4 as a function of w and product of N and D_{mean} (diameter concentration). (b) S_{QSS} as a function of TAS normalized saturation adjustment length ($L_{\text{adjust-normalized}}$) and diameter concentration (colored as mm cm^{-3}). Blue dashed line marks 0.1* $L_{\text{adjust-normalized}}$ and corresponds to 10 m for a mean TAS of 100 m s^{-1}. Red dash-dotted line marks 1% S_{QSS}.

Romps (2025)) of less than 3 mm cm^{-3}. These high S_{QSS} estimates are consistent with the prediction of the highest supersaturations in a cloud occurring with large vertical velocities and extremely low diameter concentrations (Romps, 2025). Note that the effect of vertical velocity is much stronger on the estimated S_{QSS} at smaller diameter concentrations than at larger concentrations.

However, the magnitude of the high S_{QSS} may be questionable at very low (<1 mm cm^{-3}) diameter concentrations due to the inverse relationship defined in Equation 4. To review the application of the quasi-steady state assumption in such instances, the saturation adjustment length scale (L_{adjust}) is considered. L_{adjust} can be approximated as a product of the updraft (w) and saturation adjustment timescale (τ_{adjust}) for each 1-Hz sample as previously used in Romps (2025). The τ_{adjust}, also referred as time of phase relaxation (Korolev & Mazin, 2003), is the characteristic timescale that governs how quickly the supersaturation in a cloud parcel adjusts towards its quasi-steady value. The τ_{adjust} is calculated using equation 17 from Korolev and Mazin (2003) and is applicable to those parts of cloud where large updraft and small diameter concentrations coexist, which is a region where the effect of updrafts on supersaturations may be significant. The L_{adjust} is further normalized with the measured TAS to remove the impacts of varying TAS. Figure 5b shows the scatter of the derived S_{QSS} for TAS normalized saturation adjustment length scales ($L_{\text{adjust-normalized}}$) with marker colors indicating corresponding diameter concentrations. If the TAS is assumed to be 100 m s^{-1} then a $L_{\text{adjust-normalized}}$ of 0.1 will correspond to 10 m (dash blue line). Figure 5b shows that most S_{QSS} less than 1% were estimated where $L_{\text{adjust-normalized}}$ was below 0.1, that is, shorter than ~10 m. This result is consistent with Romps (2025), who found no length scales exceeded 20 m and supersaturations were less than 1%. But for points with $L_{\text{adjust-normalized}}$ values greater than 0.1 in this study, S_{QSS} extends beyond 1% with a strong median updraft strength of 8.8 m s^{-1} and a low median diameter concentration of only 1.4 mm cm^{-3}. Because of strong updrafts and low diameter concentrations and due to the inverse relationship, points with supersaturation exceeding 1% have longer τ_{adjust} and larger $L_{\text{adjust-normalized}}$. The mean (median) L_{adjust} for high (>1%) S_{QSS} samples was 29 m (25 m) and the mean (median) τ_{adjust} for same points was 4 s (2.9 s). Figure 5b shows that the individual $L_{\text{adjust-normalized}}$ extends to values as large as 1.36 (L_{adjust} ~160 m; τ_{adjust} ~12 s) for the extreme derived S_{QSS} of 11%.

4. Results

4.1. Statistics of Key Updraft Core Microphysics

Median values from each updraft core are emphasized in the following sections to mitigate the influence of the extreme outliers and to ensure statistical robustness of the conclusions, irrespective of the number of observations available in each updraft core. The statistical distributions of four key microphysical parameters, namely $N_{<50}$, LWC$_{\text{Nevzorov}}$, w, $S_{QSS,}$ and intercepted length were derived using the median values in the sampled updraft core segments and are presented using boxplots in Figure 6. The median $N_{<50}$ in the updraft cores exhibited a wide

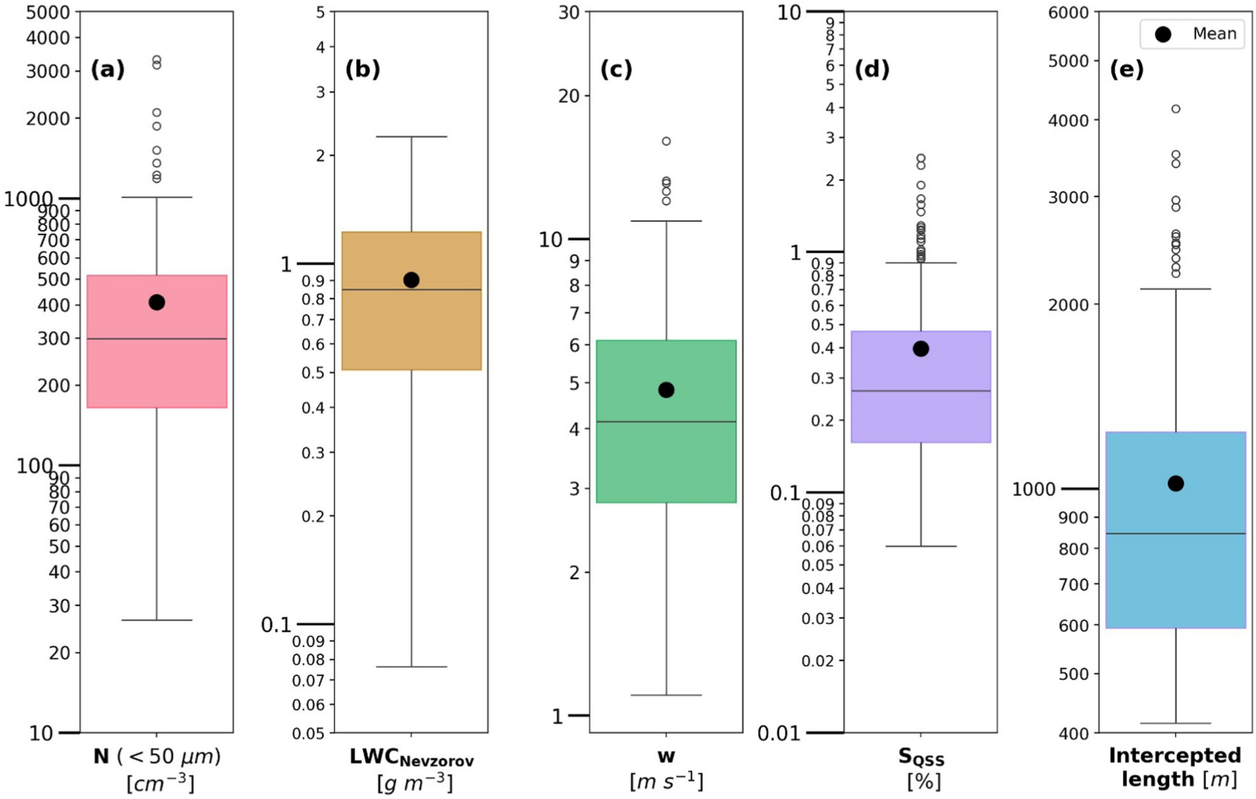

Figure 6. Boxplots shows the median statistics of (a) cloud droplet number concentrations ($N_{<50}$), (b) bulk liquid water content ($\mathrm{LWC_{Nevzorov}}$), (c) vertical velocity (w), (d) quasi-steady state supersaturations (S_{QSS}), and (e) intercepted length within 219 individual updraft core segments, based on both NRC Convair-580 and SPEC Inc. Learjet observations. Black dots represent the mean of segment median values.

range, spanning from 26 $\mathrm{cm^{-3}}$ to up to 3,300 $\mathrm{cm^{-3}}$ with a mean concentration of approximately 400 $\mathrm{cm^{-3}}$ (Figure 6a). The median bulk LWC measured using the Nevzorov probe in the updraft cores ranged from 0.08 to 2.25 g $\mathrm{m^{-3}}$ (Figure 6b) with the mean of 0.9 g $\mathrm{m^{-3}}$, and the median vertical velocity ranged from 1.1 to 16 m $\mathrm{s^{-1}}$ (Figure 6c) with the strongest measured updraft reaching nearly 28 m $\mathrm{s^{-1}}$ (not depicted in figure). Although the mean of median updraft core velocities of 4.8 m $\mathrm{s^{-1}}$ indicates the stronger nature of the sampled updraft cores, almost 93% of core median S_{QSS} estimates were less than 1%, and this aligns with supersaturations commonly derived in updrafts (Pruppacher & Klett, 1978 and references therein). The outliers observed in Figure 6d underscore the rarity of high supersaturations (>1%) in strong updraft cores. The mean value of the core median S_{QSS} was nearly 0.4%, consistent with typical supersaturations derived from cumulus cloud observations under diverse conditions (e.g., Politovich & Cooper, 1988; Prabha et al., 2011; Romps et al., 2023). The median intercepted length of the sampled updraft core segments shown in Figure 6e ranged from 415 m to about 4.2 km. Cores sampled with lengths of more than 2 km were outliers. The average intercepted length of updraft cores from this data set is about 1 km. Additionally, the sensitivity of updraft core properties to threshold choices was evaluated by varying updraft and in-cloud thresholds. Increasing updraft thresholds isolated fewer but more intense cores, resulting in higher median updraft velocities and supersaturation, consistent with the theory of quasi-steady state supersaturation ($S_{\mathrm{QSS}} \propto w$). However, stricter in-cloud thresholds had a more subtle impact on derived core statistics.

4.2. Vertical Profiles of Microphysics in Updraft Cores

To quantify the vertical variations of microphysical properties in the updraft cores, the median values in each sampled updraft core (denoted by grey dots in all panels of Figure 7) were sorted into 5 nearly equal sized groups as a function of height above cloud base, each group containing 43 to 44 updraft cores. Figure 7 shows the vertical profiles of mean, maximum and interquartile range for the median values total cloud droplet number concentration (N for $D < 50$ μm), bulk liquid water content ($\mathrm{LWC_{Nevzorov}}$), mean diameter (D_{mean}, for $D < 50$ μm),

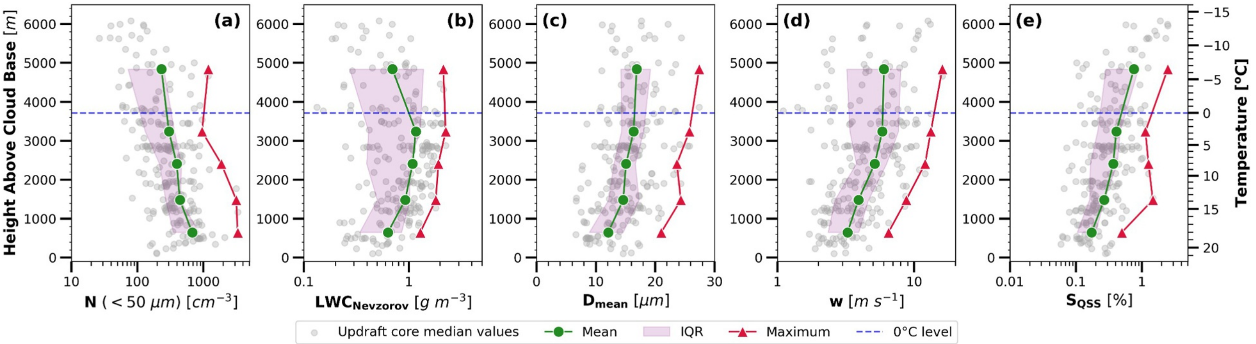

Figure 7. Each panel shows the distribution of median values within updraft cores (grey dots) derived from *in situ* probes on NRC Convair-580 and SPEC Inc. Learjet as a function of height above the cloud base. These median values for a unique updraft core segment are sorted according to the height above the cloud base and then divided into 5 nearly equal size groups each containing about 44 points. Mean (green dots and green line), Inter Quartile Range (light purple shading), and maximum (red triangle and red line) are calculated for each group and overlaid in (a) N ($D < 50$ μm), (b) $\mathrm{LWC}_{\mathrm{Nevzorov}}$, (c) D_{mean} ($D < 50$ μm), (d) w, and (e) S_{QSS} panels at the respective group averaged height above cloud base. The blue dashed line in each subplot depicts 0°C level. The secondary Y-axis on panel (e) shows temperatures to provide better physical context along the vertical profile and can be used as a common reference to (a–d) sub panels.

vertical velocity (w), and S_{QSS} sampled in total of 219 updraft cores. The interquartile range (IQR) of all variables increased with height above the cloud base, highlighting the large variability in the microphysics of deep convective clouds at lower temperatures. In Figure 7a, the mean $N_{<50}$ decreases from about 700 cm^{-3} near the cloud base to about 200 cm^{-3} near the highest sampled levels, consistent with the action of collision coalescence within the updraft core and entrainment of dry air. Figure 7b shows that the mean $\mathrm{LWC}_{\mathrm{Nevzorov}}$ increases from 0.63 g m^{-3} near the cloud base to 1.17 g m^{-3} at 3-km height above the cloud base, and this tendency is consistent with droplet growth due to condensation during adiabatic ascent. It then decreases to 0.7 g m^{-3} as the temperatures inside the core start to fall below 0°C. The mean diameter initially increased from 12 μm at the cloud base to 16 μm at 3-km height above the cloud base and then remained nearly constant above (Figure 7c). The mean updraft velocity increases with height above the cloud base from 3.25 m s^{-1} to up to 6 m s^{-1} (Figure 7d), nearly doubling within the first 3 km of core ascent indicating rapid convective growth within the sampled updraft cores. The S_{QSS} inside updraft cores shows a steady increase with height above the cloud base (Figure 7e). The largest updraft core median S_{QSS} values, reaching up to 2.47%, were estimated at heights exceeding 5 km above cloud base, in the subzero temperature regime. The mean S_{QSS} value at this highest altitude group was 0.76%, which is almost twice as high as the overall mean S_{QSS} (0.4%) as previously shown in Figure 6d. This is different from the classical trend of S_{QSS}, in which S_{QSS} increases slightly above the cloud base and then decreases asymptotically with height, consistent with aerosol nucleation near the cloud base and their subsequent growth during adiabatic ascent (Howell, 1949; Politovich & Cooper, 1988). Similar analysis repeated using data from each aircraft separately found no qualitative differences in observed trends with altitude.

4.3. High Supersaturation Case Studies

The S_{QSS} boxplot in Figure 6d shows that median S_{QSS} in the updraft cores exceeding 1% are rare. Locally, the supersaturations in intense updrafts may increase with height above cloud base due to rapid cooling during ascent, which limits the sufficient time for droplets to consume excess water vapor (Pruppacher & Klett, 1978). Thus, high values of S_{QSS} at higher levels are likely due to first, abundant condensed water vapor due to strengthening updrafts above the cloud base (Figure 7d) and second, due to reduced number concentrations (Figure 7a) of nearly similar size of cloud droplets (Figure 7c) reducing the effective sink of the available water vapor. Occurrences of such high S_{QSS} are required for the nucleation of higher aerosol loads (Fan et al., 2007; Igel & van den Heever, 2021) through secondary nucleation of ultrafine aerosols above cloud base (Fan et al., 2018). To further investigate the potential for the invigoration hypothesis, isolated instances of updraft core median S_{QSS} of up to 2.47% case (from LRF10) and 1 Hz S_{QSS} estimation of as high as 11% case (from CRF06) are discussed in the following subsections with respective meteorological context.

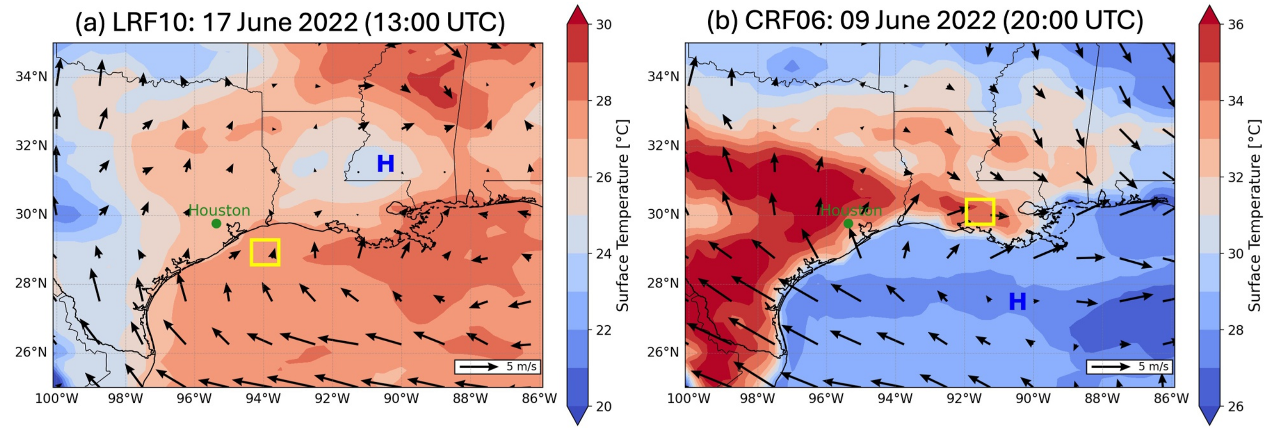

Figure 8. Sub-synoptic surface conditions present on (a) 17 June 2022 at 13:00 UTC and (b) 09 June 2022 at 20:00 UTC, approximately 30–60 min before the time of sampling convection, respectively. Filled contour shows 2-m surface temperatures obtained from the ERA5 data set. Letter "H" denotes the high pressure at the surface. The wind barbs show a wind pattern at 10 m above the surface obtained from the ERA5 data set. The green dot shows the location of Houston, Texas. Yellow squares show the approximate location of sampled cloud updraft cores for each case.

4.3.1. High Supersaturation Case From SPEC Learjet Observations

The SPEC Learjet sampled early morning deep convection in a moist and pristine environment over the Gulf during LRF10. Figure 8a shows temperature, pressure, and winds from the European Centre for Medium-Range Weather Forecasts reanalysis (ERA-5) reanalysis data set near the surface prior to the in situ observations. The 2-m temperature contours indicate the presence of a warm surface airmass over the Gulf. The presence of surface high pressure over Mississippi created a sub-synoptic anticyclonic circulation, resulting in the early onset of pristine southeasterly winds over the Gulf and onshore winds over the Texas and Louisiana coastlines. These prevailing southeasterly winds carry warm, moist air over the sampled domain, creating favorable conditions for the development of deep convective clouds. The yellow square box in Figure 8a shows the approximate location of the storm cells sampled by the Learjet in the context of surface observations and the blue box in Figure 4 denotes the exact locations of the updraft cores sampled between 13 and 14 UTC.

Figures 9a–9c shows vertical cross sections of reflectivity, mean Doppler velocity, and spectral width from the airborne Ka-band radar, respectively. These observations were taken approximately 6 km above mean sea level, as indicated by the flight track (solid black line). Two high reflectivity signatures indicate that the SPEC Learjet aircraft sampled two individual strong thunderstorm cells at approximately 13:34:10 UTC and 13:35:50 UTC. The mean Doppler velocity below 6 km was predominantly negative (downdrafts), but the very high spectral width up to 6 m s^{-1} indicates significant fluctuations in the magnitude of mean Doppler velocities. Note that the sign of mean Doppler velocities is flipped for the beam above the aircraft (Zenith direction), so positive (red) are always updrafts, and negative (blue) are downdrafts. Additionally, Ka-band radar signals are attenuated below 3 km in the first cell and below 5 km in the second cell, which is expected due to the attenuation of short-wavelength radar signals in strong thunderstorm cores.

The PPI scans of NEXRAD radar from Houston (KHGX) covered the complete precipitation lifecycle of these isolated storms, complementing the high-resolution cross-sections snapshots from the airborne platform. The first 35 dBz echoes at 0.5-degree elevation from both cells were observed at 13:01 UTC and 13:23 UTC, whereas the last 35 dBz echoes were at 14:02 UTC and 14:09 UTC, respectively. After comparing these times with the time of in situ sampling, the first cell can be classified as relatively mature and the second cell as in a developing stage of its precipitation lifecycle. This life cycle stage approximation is further supported by investigating in situ vertical velocities and LWC as shown in Figures 9d and 9e, respectively. The first cell contained penetrative downdrafts ($w < -1$ m s^{-1}) with limited updraft strength (maximum $w < 10$ m s^{-1}) and limited $\mathrm{LWC}_{\mathrm{Nevzorov}}$ (<0.5 g m^{-3}), indicating a mature stage in the thunderstorm lifecycle. On the other hand, the second cell is assumed to be in a developing stage due to the relatively stronger updraft strengths ($w > 10$ m s^{-1}), lack of any penetrative downdrafts and considerably larger LWC (>1 g m^{-3}). In addition, the hydrometeor images from the 2DS shown for the highest supersaturation instances in Figure 10 are helpful in identifying the stage of lifecycle. Figures 10a and 10b from two penetrations in the first cell show a significant presence of ice with only a few supercooled

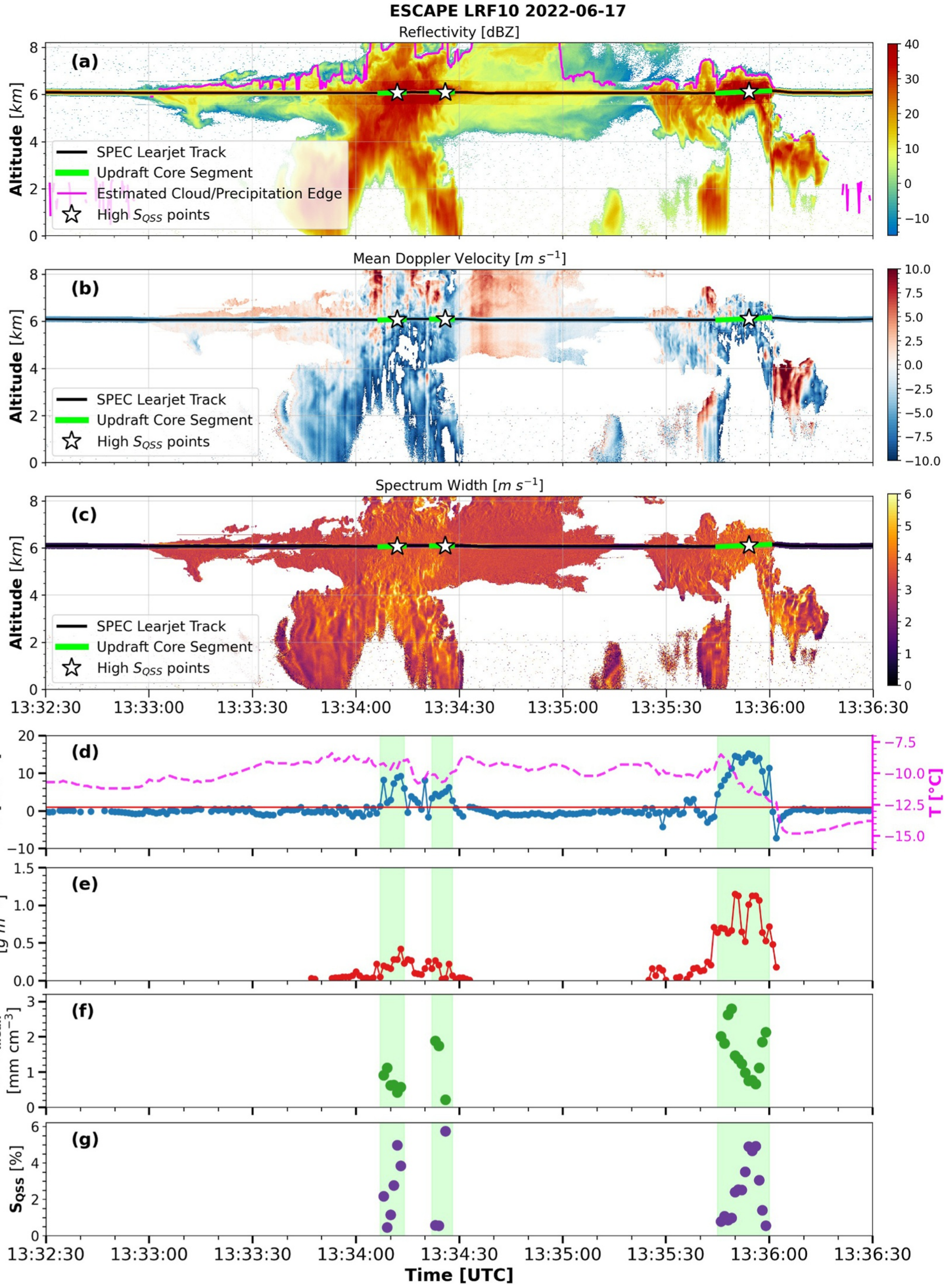

Figure 9. Time series from multiple instruments on the SPEC Learjet in three high S_{QSS} updraft core segments. Panels (a–c) show the vertical cross section of reflectivity, mean doppler velocity, and spectrum width from airborne Ka-band precipitation radar, respectively. White stars show the highest supersaturations in updraft core segments overlaid on radar data. The magenta line in reflectivity panel (a) is the nearest identified cloud/precipitation edge above the aircraft using 0 dBz threshold from the Ka-band radar. The black line is the flight track. Panels (d–g) show in situ timeseries of w, $\mathrm{LWC_{Nevzorov}}$, $N \cdot D_{\mathrm{mean}}$ (diameter concentration), and S_{QSS}, respectively. The red solid line in (d) corresponds to a vertical velocity of 1 m s^{-1} to highlight updrafts. Magenta dashed line in panel (d) depicts in situ temperature measurements. Shaded green segments in all panels indicate the updraft core segments identified using thresholds defined in Section 3.1. S_{QSS} at edges of updraft cores not shown since these points are excluded due to the limitation of the quasi-steady state assumption.

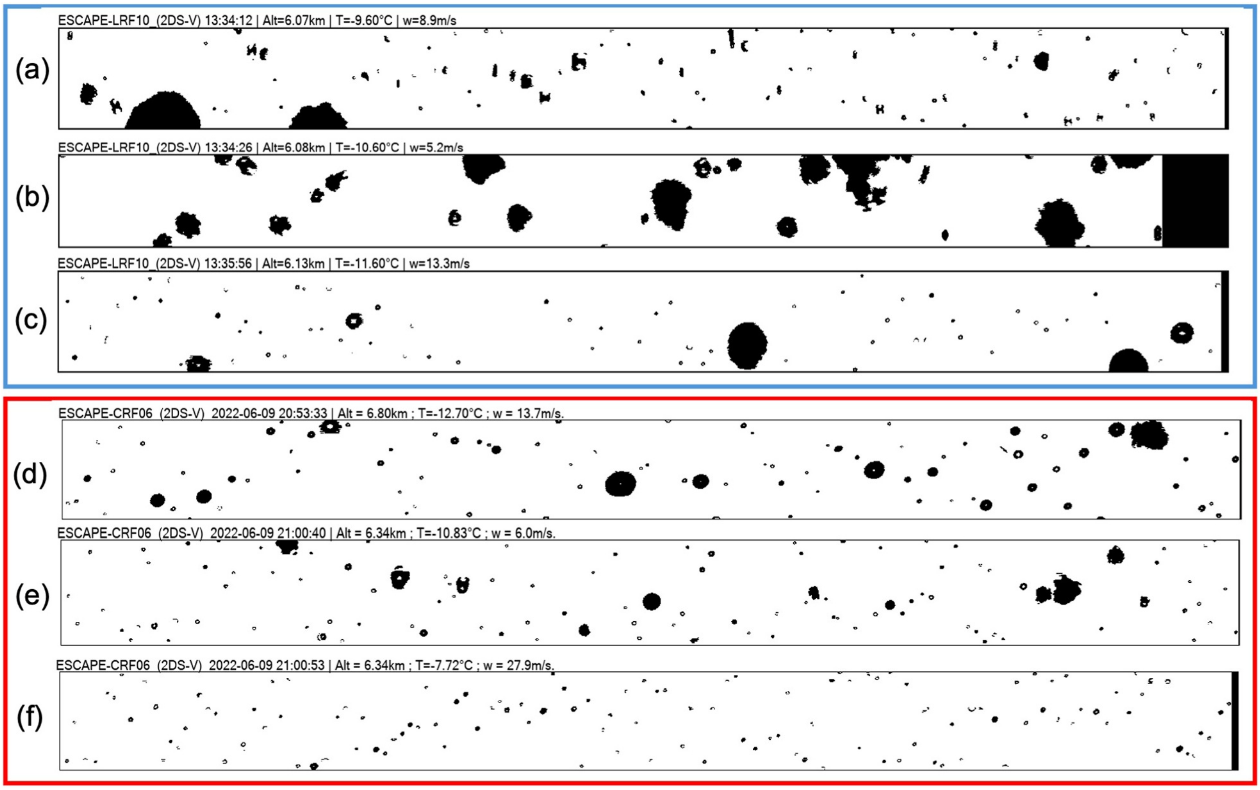

Figure 10. Selected images of hydrometeors captured at the time of maximum supersaturation in each of the six updraft core segments are depicted in Figures 9 and 12 using a 2DS V channel probe. Blue and red boxes group segments from the SPEC Learjet (Figure 9) and the NRC Convair-580 (Figure 12) platforms, respectively. For scale, the height of each subpanel is equivalent to 1.28 mm. For additional reference, hydrometeors with smoother outer edges can be approximated to be in a liquid phase while those with irregular edges are in an ice phase. However, it is important to note that this classification approximation is uncertain for smaller hydrometeors and those captured out of focus (resulting in donut-like images). The time, altitude, temperature, and w details for each sub-panel are as follows: (a) 17 June 2022 13:34:12 UTC, 6.07 km, −9.6°C, 8.9 m s^{-1}; (b) 17 June 2022 13:34:26 UTC, 6.08 km, −10.6°C, 5.2 m s^{-1}; (c) 17 June 2022 13:35:56 UTC, 6.13 km, −11.6°C, 13.3 m s^{-1}; (d) 09 June 2022 20:53:33 UTC, 6.8 km, −12.7°C, 13.7 m s^{-1}; (e) 09 June 2022 21:00:40 UTC, 6.34 km, −10.83°C, 6.0 m s^{-1}; (f) 09 June 2022 21:00:53 UTC, 6.34 km, −7.72°C, 27.9 m s^{-1}.

cloud droplets, indicating a prevalent mixed phase in typical mature storms. On the other hand, Figure 10c shows the dominating presence of supercooled liquid droplets with only a few ice particles, suggesting warm phase dominated microphysics as expected in the early developing stages of convection. Note that the presence of penetrative downdrafts in the first cell caused one thunderstorm core to be identified as two separate updraft core segments (each segment highlighted in green colors) due to the method previously described in Section 3.1. However, such a rare case of misidentification does not affect the discussion in a qualitative manner.

A careful interpretation of diameter concentrations is necessary, as they are strongly influenced by the number concentrations due to their larger numerical variability than the drop diameters. Cloud droplet probes nominally sample a limited range of cloud diameters from 2 μm to up to 50 μm, but their concentrations may vary from less than 10 cm^{-3} to more than 1,000 cm^{-3}. Therefore, large diameter concentrations can be more likely in the presence of numerous small droplets than a few large droplets. The maximum diameter concentrations (Figure 9f) in the developing cell were higher by up to 1 mm cm^{-3} compared to the mature cell. However, the minimum diameter concentrations are of particular interest due to its inverse relationship with the derived S_{QSS} given in Equation 4. The derived S_{QSS} at 1 Hz are shown in Figure 9g and are as high as 5% in both cells. The median S_{QSS} of the first and third updraft core segments, corresponding to the first and second storm cells, were 2.47% and 2.46%, respectively. These median supersaturations are the highest from ESCAPE and are significantly higher than values estimated in prior studies (Romps, 2025). Since the first storm cell was divided into two separate updraft cores, the median S_{QSS} combining both segments from the first cell was 2.17%, which is still very high. But the segment through this matured cell had a significant presence of ice particle concentrations as shown in Figures 10a and 10b, which were not considered in the calculation of S_{QSS}. Therefore, it is possible that the S_{QSS}

of 2.17% would be lower than this calculated value due to an additional supersaturation sink caused by ice hydrometeors. A simple comparison of median supersaturations in the developing cell (2.46%) and mature cell (2.17% or potentially lower) in a similar thermodynamic environment suggests that developing cells with stronger updrafts exhibit higher supersaturations compared to developed cells. This is consistent with the storm in the mature stage having relatively weaker updrafts ($w < 10$ m s^{-1}). Korolev and Mazin (2003) reported that in mixed phase conditions, supersaturation is mainly controlled by liquid droplets when the ice particle diameter concentration is lower. Therefore, considering this argument, the S_{QSS} of 2.46% would not be affected substantially due to the dominating presence of supercooled liquid water droplets over only a few ice particles (see Figure 10c).

The uncertainty in estimated S_{QSS} was quantified by propagating measurement uncertainty through the quasi-steady state formulation defined in Equation 4. A Monte Carlo approach was applied to a baseline updraft state to capture the complete distribution of plausible S_{QSS} values. The baseline updraft state was defined as the closest 1-Hz S_{QSS} value to the core median S_{QSS} and the corresponding values of vertical velocity (w), cloud droplet number concentration (n), mean droplet diameter (D), pressure (p), and temperature (T). Therefore, for the second storm cell with a median S_{QSS} of 2.46%, the baseline updraft state was considered to be at the closest 1-Hz S_{QSS} value of 2.40%. The w, n, D, p, and T corresponding to 2.40% S_{QSS} were 14.6 m s^{-1}, 58 cm^{-3}, 25.2 μm, 467.3 hPa, and 263.15°K, respectively. The measurement uncertainties were assumed from the instrument manuals for subsequent analysis and were w (±0.5 m s^{-1}), p (±1.3 hPa), and T (±0.5°K). Baumgardner et al., 2017 describe propagated uncertainties to derive n and D as 10%–30% and 10%–50% respectively. Therefore, the worst-case scenario was considered by assuming relative uncertainties of n to be 30% and D to be 50%. The w, p, and T were perturbed additively using Gaussian distributions centered on the observed values with standard deviations corresponding to instrument uncertainty. n and D were perturbed multiplicatively using lognormal distributions to reflect their strictly positive nature and fractional measurement uncertainty, respectively. For a given state, measurement uncertainty was determined by generating an ensemble of 20,000 perturbed realizations of (w, n, D, p, T) to ensure that higher percentiles are numerically stable, which is particularly important for high-supersaturation regimes. S_{QSS} was recalculated for each realization using the same analytical formulation (Equation 4) as for the base estimate, producing a probability distribution of S_{QSS} values for each state. From this distribution, the percentile bounds (5th, 50th, and 95th percentiles) were computed. Consequently, the median S_{QSS} from the Monte Carlo samples was 2.41%, with 5th and 95th percentiles of 0.96% and 6.06%, respectively. This indicates significant uncertainties in the estimated S_{QSS} due to measurement error propagation.

4.3.2. Extreme Supersaturation Case From NRC Convair-580 Observations

The NRC Convair aircraft was sampling an isolated thunderstorm on CRF06 on 09 June 2022 at the time of the estimated 11% S_{QSS}. The surface temperatures and 10-m winds from ERA5 reanalysis data at 20 UTC are shown in Figure 8b. A much larger surface temperature contrast was present on this day compared to the previous case. A weak surface high over the Gulf, together with a confluence band aligned parallel to the Louisiana-Mississippi coastline, resulted in strong onshore winds over the Texas-Louisiana coastline. Therefore, low-level winds near sampled thunderstorms were westerly northwesterly owing to the sub-synoptic scale flow pattern. The yellow box in Figure 8b indicates the approximate location, and the orange box in Figure 4 shows the exact geographical location of the storm cores discussed in this case study.

Sampling was conducted at multiple levels with the highest median S_{QSS} of 1.9% estimated on the highest altitude leg at an altitude of 6.8 km and a temperature of −13°C. The ambient aerosol observations in Figures 11a and 11c were taken in the upwind direction after sampling the thunderstorm at 800 m above sea level and approximately 300 m below cloud base. The back trajectory analysis shown in Figure 11b was performed with the Hybrid Single-Particle Lagrangian Integrated Trajectory model (HYSPLIT, Stein et al., 2015) v5.3.2 model initialized using the Global Forecast System (GFS) 0.25° meteorological data set. Although winds were westerly near the thunderstorm cloud base (∼1,100 m), the back-trajectories indicate that the actual airmass source was from over the Gulf, which is consistent with the meteorological context presented in Figure 8b. This marine air mass spent less than 12 hr over the coastal region of Louisiana before being ingested into the thunderstorm. The NRC Convair-580 was mounted with aerosol probes including Condensation Particle Counter (CPC), Ultra High Sensitivity Aerosol Spectrometer (UHSAS) and three CCN counters maintained at three unique supersaturations. More details about aerosol measurements, their limitations and the sampling strategy adopted during ESCAPE can be found in Kollias et al., 2025. Figure 11a shows N_{CPC} (color-coded dots) sampled westward away from the thunderstorm

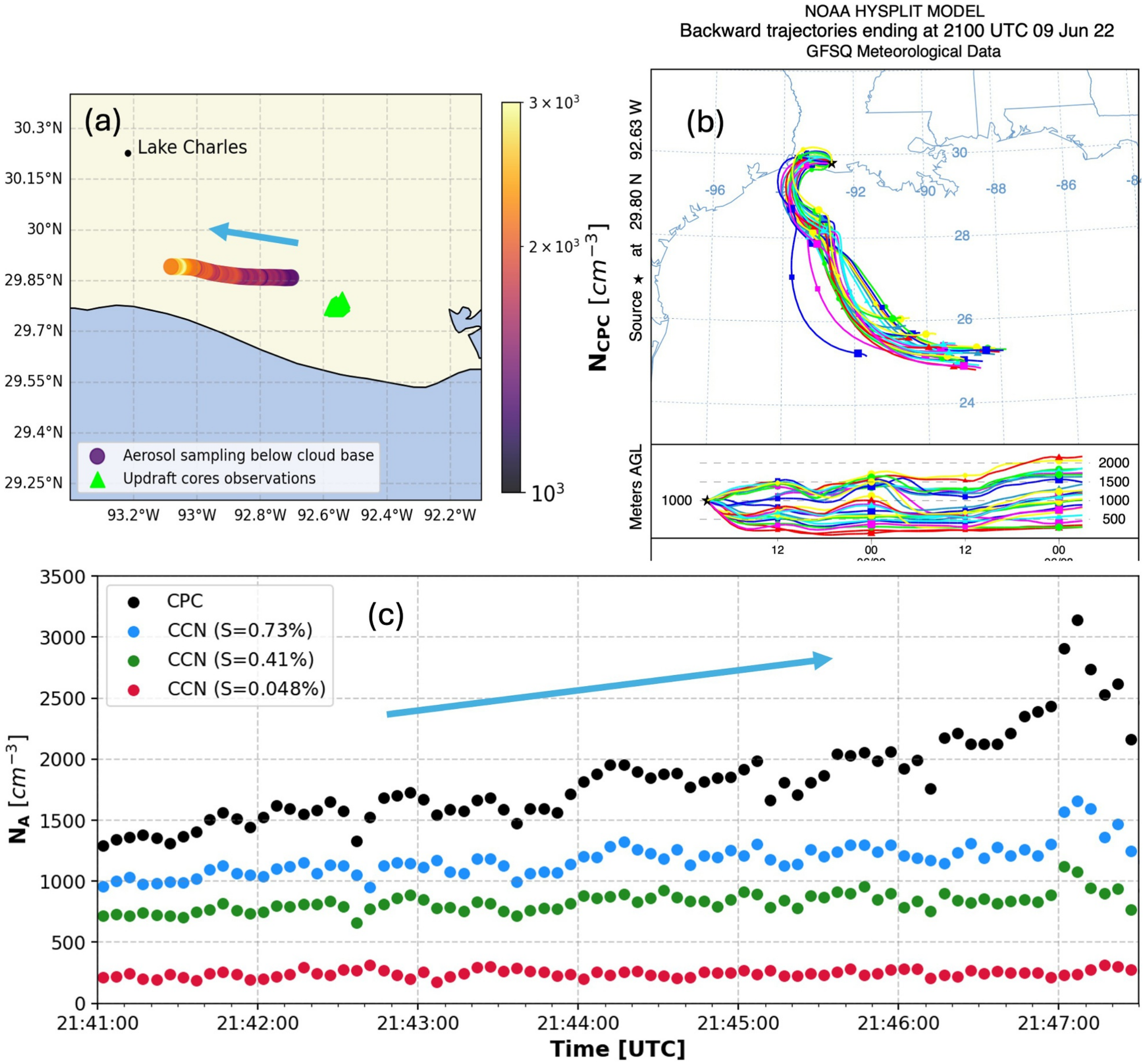

Figure 11. Aerosol measurements for context of flight CRF06 on 09 June 2022 when S_{QSS} of 11% was estimated. (a) Shows in situ aerosol concentrations measured by the condensation particle counter (CPC) onboard the NRC Convair-580 below cloud base at an altitude of 800 m and temperature of 24°C in the upwind direction after sampling an isolated thunderstorm (green triangles) at approximately 21:00 UTC. The blue colored arrow indicates the aerosol sampling direction. (b) Shows the NOAA HYSPLIT backward trajectory at 21 UTC showing the airmass had an origin over the Gulf. (c) Total aerosol number concentration N_{CPC} (Black scatter) and CCN concentration at supersaturations (S) of 0.048% (Red), 0.41% (Green) and 0.73% (Blue) with arrow indicating upwind direction with left side of the time series closest to cloud updraft core observations.

(green triangles) and Figure 11c shows the corresponding time series from different onboard aerosol instruments. The N_{CPC} in the sampled airmass substantially decreased (144%) from more than 3,000 cm^{-3} to about 1,300 cm^{-3} closer to the thunderstorm. However, the cloud condensation nuclei (CCN) concentrations measured at three constant supersaturations changed to a lesser extent with a slight decrease of 74%, 70% and 78% for the supersaturations of 0.048%, 0.41% and 0.73%. The aerosol and CCN concentrations are representative of the rural background for this region (Roberts et al., 2026).

The NEXRAD (KLCH) radar located in the vicinity of the storm detected its first 35 dBZ echo at 20:16 UTC and last echo at 21:37 UTC. Thus, when the NRC Convair-580 started sampling at 20:53 UTC, it was in the late growth stage of precipitation lifecycle at 6 km altitude. The NRC Convair-580 then gradually spiraled down and transversed through the core 5 times every 3–4 min. Only the first and third transects are discussed in detail because they contained the highest 1-Hz S_{QSS} and strongest updrafts, respectively. Figure 12 shows airborne X-band radar vertical cross sections and microphysics time series for two strong updraft core segments of the same storm separated by less than 7 min. The Nyquist velocity (V_{Nyquist}) for the onboard X-band radar was 13.3 m s^{-1}, so ambiguous velocities (V_{Observed}) were numerically unfolded using Equation 5 to obtain mean Doppler velocities (V_{True}). The term "n" in Equation 5 is an integer that represents the number of times the velocity has been folded. The sign of the mean Doppler velocities (12b, 12i) from the zenith pointing beam was flipped to consistently define positive (red) velocities as updrafts and vice versa.

$$V_{\mathrm{True}} = V_{\mathrm{Observed}} + n \times 2V_{\mathrm{Nyquist}} \tag{5}$$

Figures 12a–12g corresponds to the first transect, and Figures 12h–12n corresponds to the second and third transect through the storm. The vertical cross section of radar reflectivity (Figure 12a) shows that the aircraft transect at 6.8 km was through the top of one discrete reflectivity core and at least 1.5 km below the estimated cloud/precipitation edge, which corresponds to a 14 dBz threshold. Figure 12b shows that mean Doppler velocities in the storm were mostly negative, but an elevated strong updraft core was intercepted between 5 and 7.5 km. The depth of the updraft core below 4 km cannot be robustly confirmed due to the signal attenuation. The presence of high spectral widths up to 6 m s^{-1} (Figure 12c) below the transect indicates the presence of strong turbulence throughout the depth of the updraft core. In-situ observations revealed vertical velocities up to 21 m s^{-1} (Figure 12d), LWC$_{\mathrm{Nevzorov}}$ up to 0.8 g m^{-3} (Figure 12e), diameter concentration up to 2.4 mm cm^{-3} (Figure 12f), and S_{QSS} up to nearly 11% (Figure 12g). An S_{QSS} of 11.2% was estimated when the vertical velocity was at 13.68 m s^{-1}, and the diameter concentration was extremely low at just 0.29 mm cm^{-3}. The median S_{QSS} of this segment was also very high at 1.9%. The intercepted length of this updraft core segment calculated using the product of true air speed (TAS) and the total sampled duration in seconds were 1.68 km. The uncertainty in S_{QSS} of 11.2% due to measurement errors can be calculated using the methodology outlined in Section 4.3.1. By assuming a baseline updraft state of 1 Hz observations corresponding to 11.2%, the resulting 5th and 95th percentiles from Monte Carlo samples were 4.48% and 28.23%, respectively. Note that this range is substantially larger for the 11.2% supersaturation estimate compared to the 2.4% supersaturation estimate from the Learjet observations. The second transect through the same storm (not discussed in detail here) 3 min later had a slightly wider updraft core (intercepted length of 2.07 km) with maximum 1 Hz S_{QSS} up to 2.16% and high median S_{QSS} of 1.67%.

Nearly 7 min after sampling the first transect, an updraft at 6.4 km altitude was sampled and was widest (∼2.4 km) and strongest with vertical velocities up to 28 m s^{-1} (Figure 12k). The reflectivity cross section in Figure 12h indicates that aircraft sampled near the top of the high reflectivity core and much closer to the cloud/precipitation edge than the first transect. Mean Doppler velocities (Figure 12i) show persistent elevated updraft regions 5–8 km surrounded by downdrafts, while large spectral widths (Figure 12j) indicate consistently strong turbulence below the transect. Although vertical velocities remained consistently above 1 m s^{-1}, the LWC$_{\mathrm{Nevzorov}}$ for one second dropped below 0.01 g m^{-3} causing one large updraft core to be identified as two individual updraft core segments. The maximum LWC$_{\mathrm{Nevzorov}}$ was nearly double that of the first transect, up to 1.6 g m^{-3} and the diameter concentration was also larger up to 2.8 mm cm^{-3}. The maximum S_{QSS} of 3.05% was estimated with the strongest updraft of 28 m s^{-1} and diameter concentration of 2.14 mm cm^{-3}. If it is assumed that the aircraft penetrated the strongest part of the storm in all core segments near 6 km, then perhaps this case of extreme supersaturations (11.2%) followed by stronger peak updrafts (28 m s^{-1}) with additional diameter concentrations and lowered peak supersaturation (3%) may be consistent with the condensational invigoration hypothesis.

4.4. Probability of Finding High Supersaturations in Updraft Cores

To determine the viability of the condensational invigoration hypothesis, it is important to know the frequency at which high supersaturations occur and the conditions under which they occur. As Figure 6d suggests, the occurrence of high supersaturations ($S_{\mathrm{QSS}} > 1\%$) in strong updraft cores is rare, and therefore, a bootstrapping approach (e.g., Efron & Tibshirani, 1994) is adopted to estimate the conditional probability of such events under different temperature and updraft regimes. Bootstrapping is well suited here because the statistical distribution of uncertainty in S_{QSS} estimations is not known a priori, and this method provides a nonparametric way to generate confidence intervals by resampling with replacement. A grid of environmental conditions is defined by vertical velocity thresholds (w_{min}; {1, 2, 4, 6, 8, 10} m s^{-1}) and temperature bins (T_{low}, T_{high}; {(−∞, −20], (−20, −10],

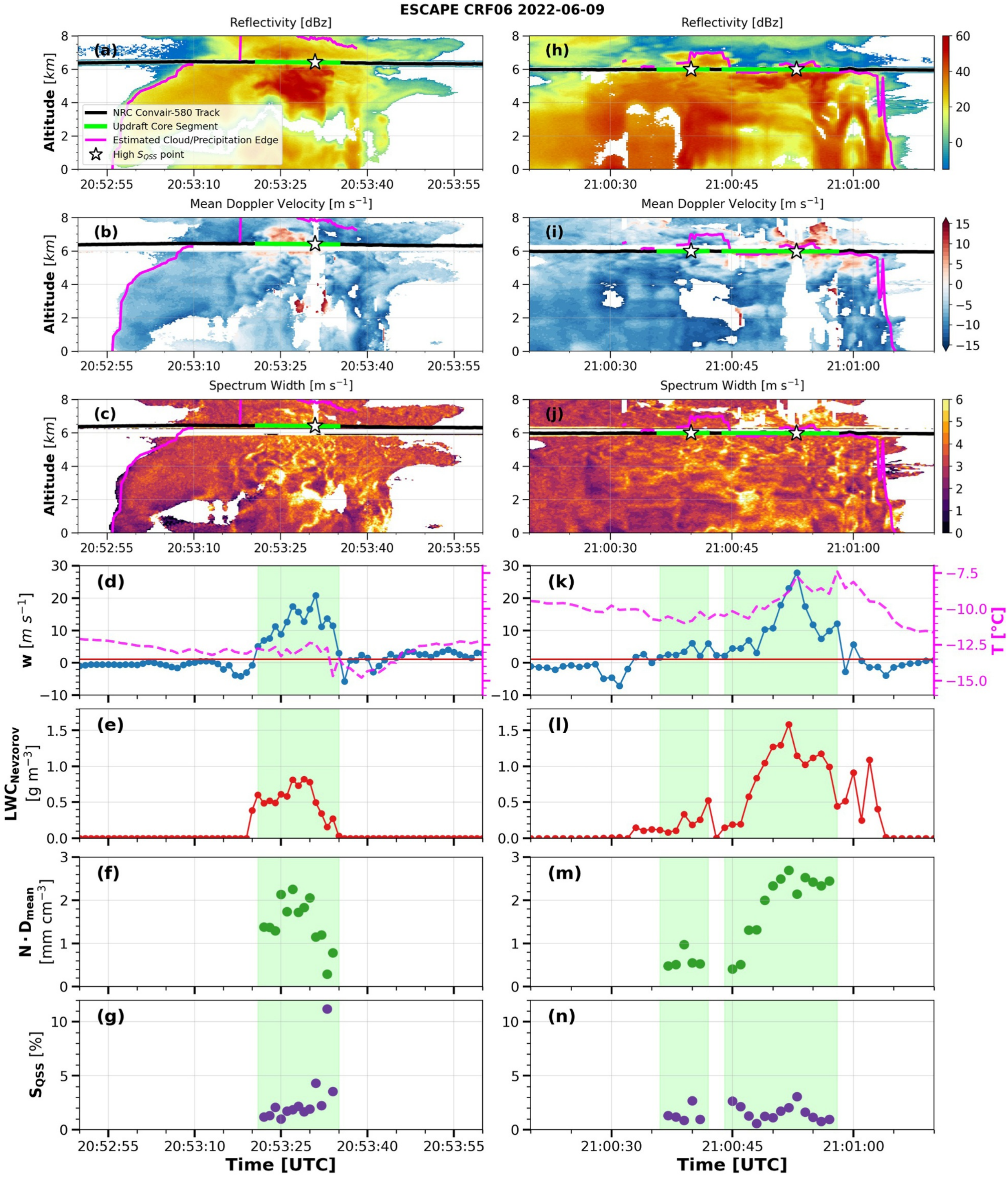

Figure 12. First transect between 20:53:21 and 20:53:35 UTC (a–g, left column) and second and third transect between 21:00:36 and 21:00:58 UTC (h–n, right column) through strong and deep updraft cores sampled by the NRC Convair-580 during CRF06 on 09 June 2022. (a and h) show reflectivity; (b and i) show mean Doppler velocities; and (c and j) show spectrum widths from the airborne X-band radar. (d, k), (e, l), (f, m), and (g, n) show in situ measured time series of vertical velocities (blue), LWC measured by Nevzorov (red), diameter concentration derived from CDP size distributions (green), and S_{QSS} estimated using Equation 4 (purple), respectively. The red horizontal line in (d, k) is for $w = 1$ m s^{-1}, indicating any scatter above it as an updraft. Magenta dashed line in panels (d, k) depicts in situ temperature measurements. Green highlights are the identified updraft core segments using methods described in Section 3.1. White stars on the radar derived variable (a–c, h–j) indicate an approximate location of high supersaturation instances. The magenta line in the same panel is the nearest estimated cloud/precipitation edge found using 14 dBz threshold from the X-band radar.

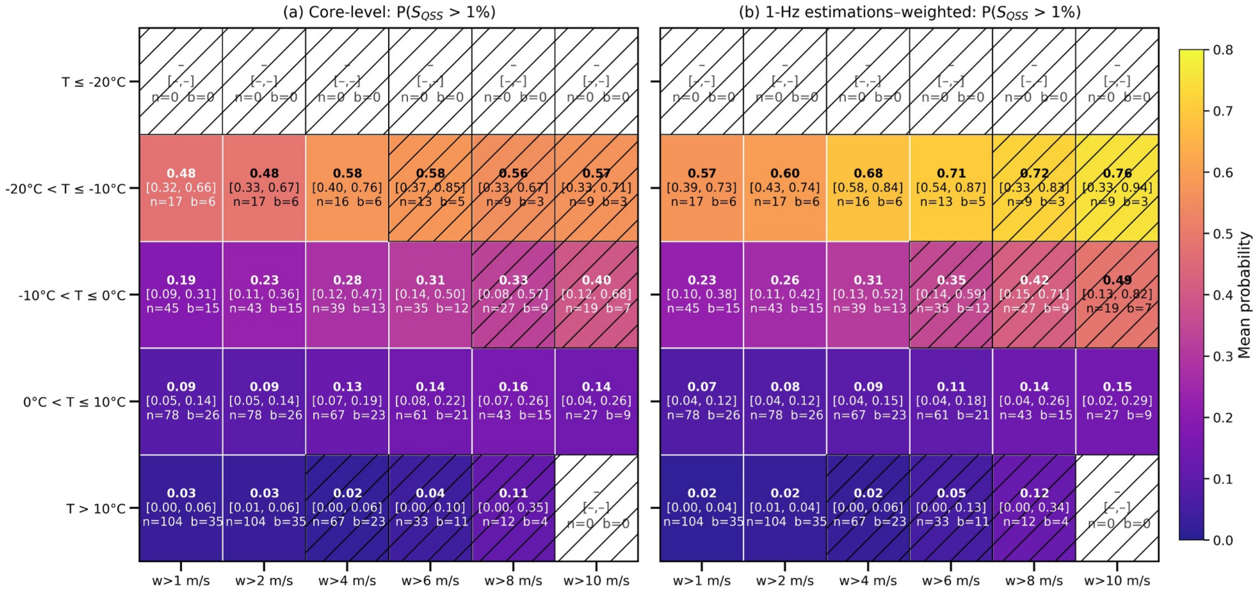

(a) Core-level: P(S_{QSS} > 1%)

	w>1 m/s	w>2 m/s	w>4 m/s	w>6 m/s	w>8 m/s	w>10 m/s
T ≤ -20°C	– [–,–] n=0 b=0	– [–,–] n=0 b=0	– [–,–] n=0 b=0	– [–,–] n=0 b=0	– [–,–] n=0 b=0	– [–,–] n=0 b=0
-20°C < T ≤ -10°C	0.48 [0.32, 0.66] n=17 b=6	0.48 [0.33, 0.67] n=17 b=6	0.58 [0.40, 0.76] n=16 b=6	0.58 [0.37, 0.85] n=13 b=5	0.56 [0.33, 0.67] n=9 b=3	0.57 [0.33, 0.71] n=9 b=3
-10°C < T ≤ 0°C	0.19 [0.09, 0.31] n=45 b=15	0.23 [0.11, 0.36] n=43 b=15	0.28 [0.12, 0.47] n=39 b=13	0.31 [0.14, 0.50] n=35 b=12	0.33 [0.08, 0.57] n=27 b=9	0.40 [0.12, 0.68] n=19 b=7
0°C < T ≤ 10°C	0.09 [0.05, 0.14] n=78 b=26	0.09 [0.05, 0.14] n=78 b=26	0.13 [0.07, 0.19] n=67 b=23	0.14 [0.08, 0.22] n=61 b=21	0.16 [0.07, 0.26] n=43 b=15	0.14 [0.04, 0.26] n=27 b=9
T > 10°C	0.03 [0.00, 0.06] n=104 b=35	0.03 [0.01, 0.06] n=104 b=35	0.02 [0.00, 0.06] n=67 b=23	0.04 [0.00, 0.10] n=33 b=11	0.11 [0.00, 0.35] n=12 b=4	– [–,–] n=0 b=0

(b) 1-Hz estimations–weighted: P(S_{QSS} > 1%)

	w>1 m/s	w>2 m/s	w>4 m/s	w>6 m/s	w>8 m/s	w>10 m/s
T ≤ -20°C	– [–,–] n=0 b=0	– [–,–] n=0 b=0	– [–,–] n=0 b=0	– [–,–] n=0 b=0	– [–,–] n=0 b=0	– [–,–] n=0 b=0
-20°C < T ≤ -10°C	0.57 [0.39, 0.73] n=17 b=6	0.60 [0.43, 0.74] n=17 b=6	0.68 [0.58, 0.84] n=16 b=6	0.71 [0.54, 0.87] n=13 b=5	0.72 [0.33, 0.83] n=9 b=3	0.76 [0.33, 0.94] n=9 b=3
-10°C < T ≤ 0°C	0.23 [0.10, 0.38] n=45 b=15	0.26 [0.11, 0.42] n=43 b=15	0.31 [0.13, 0.52] n=39 b=13	0.35 [0.14, 0.59] n=35 b=12	0.42 [0.15, 0.71] n=27 b=9	0.49 [0.13, 0.82] n=19 b=7
0°C < T ≤ 10°C	0.07 [0.04, 0.12] n=78 b=26	0.08 [0.04, 0.12] n=78 b=26	0.09 [0.04, 0.15] n=67 b=23	0.11 [0.04, 0.18] n=61 b=21	0.14 [0.04, 0.26] n=43 b=15	0.15 [0.02, 0.29] n=27 b=9
T > 10°C	0.02 [0.00, 0.04] n=104 b=35	0.02 [0.01, 0.04] n=104 b=35	0.02 [0.00, 0.06] n=67 b=23	0.05 [0.00, 0.13] n=33 b=11	0.12 [0.00, 0.34] n=12 b=4	– [–,–] n=0 b=0

Figure 13. Conditional probability of high supersaturations ($S_{\mathrm{QSS}} > 1\%$) as a function of updraft strength and temperature. (a) Core-level probability, computed by first determining the fraction of qualifying 1-Hz samples exceeding $S_{\mathrm{QSS}} > 1\%$ and then averaging those fractions across cores. (b) Probability based on 1-Hz high supersaturations estimates, computed as the ratio of total high-supersaturation occurrences to total qualifying 1 Hz samples across all cores. Numbers indicate mean probability with 95% confidence intervals, along with contributing core segments (n) and bootstrap blocks (b). Hatched cells fail quality control criteria (confidence interval half-width >0.20, or relative half-width >1.0, or insufficient sampling with $n < 10$ or $b < 5$). The shaded color of each grid cell corresponds to the mean probability, where brighter colors indicate higher mean probability and gray color indicate the absence of any observations for respective conditions.

$(-10, 0], (0, 10], (10, \infty)\}$°C). For a given combination of (w_{min} and T_{bin}), all points inside the core that satisfy $w > w_{\mathrm{min}}$ and $T_{\mathrm{low}} < T < T_{\mathrm{high}}$ are selected to determine the core-level conditional probability, which is computed as $p_{\mathrm{core}} = P\left(S_{\mathrm{QSS}} > 1\%;\, w > w_{\mathrm{min}}, T \in T_{\mathrm{bin}}\right)$ as shown in Figure 13a. Cores without qualifying points for a given condition were excluded only from that condition, allowing the same core to contribute under other conditions. This ensures that each conditional grid cell accumulates information from many cores while preserving the conditional nature of the estimates.

A key assumption of the bootstrap is that samples are independent. In this case, each updraft core segment is treated as an independent sample. However, segments sampled close in time or within the same thunderstorm may not be entirely independent. Adjacent updraft cores can reflect the same mesoscale environment or storm evolution. If ignored, this serial dependence would lead to an underestimation of uncertainty (too narrow confidence intervals). Therefore, an autocorrelation analysis of time-ordered updraft core segments was performed. The lag-1 second correlation was 0.31, lag-2 was 0.26, and lag-3 dropped to 0.09, suggesting moderate dependence up to two core segments apart. Based on this, a block bootstrap approach was adapted to resample blocks of three contiguous core segments with replacement across 10,000 iterations per bin instead of resampling individual cores. This preserves local temporal correlation while allowing the bootstrap to provide reliable confidence intervals. Therefore, each grid cell in Figure 13a reflects the mean conditional probability across core segments, along with 95% bootstrap confidence intervals in the brackets. Additional criteria for quality control are imposed to avoid over-interpretation of undersampled or highly uncertain results. Cells in Figure 13 are hatched when (i) the confidence interval half-width exceeds 0.20, or (ii) the relative half-width exceeds unity, or when (iii) the number of contributing cores ($n < 10$) or blocks ($b < 5$) are insufficient. Condition (i) hatches a grid cell where uncertainty in the probability estimate is ±20 percentage points or larger. The relative half-width in condition (ii) is a measure of uncertainty compared to the mean estimate and is computed by dividing the confidence interval half width by the mean probability. Any value exceeding unity for relative half-width would mean that the probability estimate could plausibly be anywhere from near 0 to near 1, which is not physically useful for any claims.

According to Figure 13a, probabilities were maximized at lower temperatures ($-20°\mathrm{C} \leq T < -10°\mathrm{C}$), particularly under strong updrafts ($w > 4\ \mathrm{m\ s^{-1}}$), where mean probabilities exceeded 0.5 with relatively constrained confidence intervals (e.g., 0.58 [0.40–0.77], $n = 16$, $b = 6$), but with broader uncertainties in higher w bins due to limited data samples (small n and b). At slightly higher but below freezing temperatures ($-10°\text{C} \leq T < 0°\text{C}$), probabilities remained non-negligible (0.19–0.31) for 2–6 m s^{-1} and were uncertain at higher w bins due to larger confidence intervals. At temperatures between 0 and 10°C, probabilities of $S_{\text{QSS}} > 1\%$ are low to approximately 0.09–0.16, but quantifiably constrained with sufficient observations and a narrow confidence interval. For temperatures higher than 10°C, the probability is negligible at 0.03 for updrafts up to 10 m s^{-1}. No qualifying cases were found for updrafts stronger than 10 m s^{-1} at $T \geq 10°\text{C}$ and for $T < -20°\text{C}$ across all updraft thresholds.

While core-level probabilities describe how frequently favorable conditions occur across updraft cores, the 1-Hz estimations weighted probability quantifies how often high supersaturations are actually estimated at the 1-Hz scale within those conditions. Therefore, to directly compare the probability structure in Figure 13a with the frequency of high-supersaturation occurrences at 1-Hz, the same conditional grid of updraft and temperature regimes (w_{min}, T_{bin}) was recomputed using a 1-Hz estimation-based probability definition (Figure 13b). For each regime, the total number of qualifying observations n_i and high supersaturation occurrences k_i with $S_{\text{QSS}} > 1\%$ are summed across all cores, and conditional probability is defined as $p_{1\text{Hz}} = \sum_i k_i \Big/ \sum_i n_i$. Note that this definition differs from the core-level probability used in Figure 13a and weights each 1-Hz observation equally to reflect the occurrence frequency of high supersaturation events within the sampled updraft environment. To ensure consistency in estimation, the same block bootstrap framework is applied, resampling contiguous core segments and recomputing the ratio of sums in each iteration.

1-Hz estimation-based probabilities (Figure 13b) exhibit a similar overall structure but are systematically higher than the core-level estimates across most regimes. For ($-20°\text{C} \leq T < -10°\text{C}$), probabilities increase from approximately 0.57 at $w > 1\text{m s}^{-1}$ to 0.71 at $w > 6\ \text{ms}^{-1}$, compared to 0.48–0.58 in the core level analysis. A similar enhancement is observed for ($-10°\text{C} \leq T < 0°\text{C}$), where probabilities reach up to ~0.31. This systematic increase indicates that high supersaturation events tend to occur in clusters of consecutive 1-Hz samples within favorable updraft cores, rather than being uniformly distributed across all cores. Consequently, while relatively few cores exhibit high supersaturation frequently, the actual frequency of occurrence at the measurement scale is substantially higher when conditions are favorable.

5. Discussion and Conclusions

Deep convective clouds were sampled at different stages in their lifecycle in a variety of meteorological conditions during ESCAPE. The NRC Convair-580 and SPEC Learjet aircraft together sampled 219 updraft core segments in the coastal regions of Texas and Louisiana. The statistics of the median values in each observed updraft core showed that updraft cores were about 1 km wide and were relatively strong as the average median vertical velocity was 4.8 m s^{-1}. The median N and bulk LWC in the updraft cores were nearly 400 cm^{-3} and 1 g m^{-3} on average, respectively. The supersaturation values were derived using in situ microphysical observations by assuming a quasi-steady state. Although the average median S_{QSS} inside cores was only 0.4%, some cores had an exceptionally high S_{QSS} with the median S_{QSS} value as high as 2.47%. All updraft cores with median $S_{\text{QSS}} > 1\%$ were statistical outliers. Vertical profiles of the microphysical variables above cloud base revealed that S_{QSS} within updraft cores increased with height above cloud base.

Therefore, to better understand the background of high supersaturation cases, two case studies were discussed: one case with the highest core median supersaturation and another with the highest estimated 1-Hz supersaturation. Both cases were found to be in relatively low concentration aerosol environments. The case studies leverage and emphasize the importance of using the synergy of multi-instrument, multi-platform observations to accurately capture the spatiotemporal context of microphysical observations. In the first case, the SPEC Learjet sampled two strong thunderstorm cells over the Gulf, one in the mature stage and the other in the developing stage. A comparison of median supersaturations from the storms suggested that under the same thermodynamic environment, the developing stage (2.46%) had higher supersaturations compared to the mature stage (2.17%). The uncertainty in the S_{QSS} estimate was quantified using propagation of measurement errors around a baseline updraft state (closest 1-Hz observation to the median S_{QSS} of 2.46%), yielding a median estimate of 2.41% with a broad 5th–95th percentile range (0.96%–6.06%), highlighting considerable uncertainty due to nonlinear sensitivity to microphysical and thermodynamic variables. In the second case, the NRC Convair-580 aircraft repeatedly sampled an isolated storm near the coast of Louisiana. The first traverse through this storm had a median-derived S_{QSS} of 1.9% with a peak of 11.2% at a strong vertical velocity of 13.68 m s^{-1}. Applying a similar uncertainty quantification framework to the extreme supersaturation case (11.2%) yielded a substantially broader 5th–95th percentile range (4.48%–28.23%), indicating that S_{QSS} uncertainty increases distinctly at higher supersaturation levels. At nearly 11% supersaturation, the hydrometeor images from the 2DS probe showed a dominating presence of supercooled liquid water even at nearly −13°C (Figure 10d) and the diameter concentration was exceptionally low at just 0.29 mm cm^{-3}. Another transect after nearly 7 min at a similar altitude, sampled peak updraft strength reaching 28 m s^{-1}. Assuming that the aircraft penetrated the strongest part of the storm in all transects, this case of extreme supersaturations followed by a stronger peak updraft strength with a higher magnitude diameter concentration and lower peak supersaturation is consistent with the condensational invigoration hypothesis. Although in-cloud measurement of ultrafine aerosol was not performed to confirm their presence or activation, only a limited increase was noted in the average concentration of small cloud droplets ($3\ \mu\mathrm{m} < D < 12\ \mu\mathrm{m}$) from 14 to 15 cm^{-3} as well as in the total N_{CDP} ($3\ \mu\mathrm{m} < D < 50\ \mu\mathrm{m}$) from 83 to 94 cm^{-3} in the two discussed transects, respectively. However, the exact transect location relative to the updraft core cannot be easily determined. Further it cannot be unambiguously inferred from observations whether the strengthened updraft in the following transect was due to invigoration or due to other meteorological forcing. Although the estimated S_{QSS} magnitude of 11% provides some evidence of the high supersaturations needed for the invigoration hypothesis, such high S_{QSS} were statistical outliers among the 219 updraft cores sampled over 9 different days, representing 52 min of 1-Hz observations within updraft cores. This indicates that either such high supersaturation pockets are naturally rare or that research aircraft are not able to sample the specific conditions where they occur. Nevertheless, the evidence of such estimations from this and earlier studies (e.g., Prabha et al., 2011) shows that additional observations under the discussed conditions are sorely needed to better identify the pockets of high supersaturations. Such sampling may be challenging, as it is possible that such pockets are dynamic and transient. Using a bootstrapping approach on 219 sampled updraft core segments (Figure 13) demonstrates that high supersaturation events are most likely in cold, strong updraft environments, with both definitions yielding consistent spatial patterns but differing in magnitude due to their statistical interpretation. The comparison between Figures 13a and 13b highlights the importance of distinguishing between core-to-core variability and within-core occurrence frequency when evaluating aerosol-cloud interaction processes. Note that this is purely a statistical result and is based on limited data using numerical techniques with no physical processes accounted for.

The limitations of employing the quasi-steady state assumption are discussed in the Methods section. However, the applicability of the quasi-steady state condition, particularly at extreme S_{QSS} is subject to debate if the relatively large values of L and τ can justify a valid quasi-steady state. Romps (2025) noted that this assumption is only applicable when the saturation adjustment length scale is significantly smaller than typical updraft length scale in case of moist convective updrafts or when it is significantly smaller than typical aerosol activation length scale in cases of all ascending air. During ESCAPE, the average intercepted length (updraft width) from both aircraft was found to be about 1 km. Although the vertical extent of convective updrafts was not calculated, it can be assumed to be at least a few km in sustained strong vertical velocities of deep convective clouds. Therefore, the estimated L_{adjust} of 160 m with a vertical velocity of 13.68 m s^{-1} for the maximum estimated supersaturation (11%) is still much smaller than typical moist updraft length scales of a few km. Consequently, the quasi-steady state assumption can still be applied here when compared with moist convective updraft length scales. However, if we are to compare it with typical aerosol activation length scales, then this assumption may not be considered valid since the aerosol activation length scales are in the order of only tens of meters (Howell, 1949; Mordy, 1959; Romps, 2025). Therefore, there can be two different sets of conclusions depending on which criterion is chosen. If moist convective updraft length scales are compared with saturation adjustment length scales, then predictions of high supersaturations by Equation 4 for strong updrafts and low diameter concentrations (Figure 5) would be valid and represent real occurrences of high supersaturations. Conversely, if aerosol activation length scales are comparable, then the saturation adjustment length scale becomes too large to justify the quasi-steady state assumption. Korolev and Mazin (2003) fundamentally interpreted S_{QSS} as an "equilibrium" supersaturation that occurs in conditions where the increase in saturation due to cooling is balanced by the droplet growth due to condensation, but is saturation equilibrium really ever achieved in strong updrafts?

Conflict of Interest

The authors declare no conflicts of interest relevant to this study.

Availability Statement

All the data from the ESCAPE are cataloged at the NCAR EOL ESCAPE data archive: https://data.eol.ucar.edu/project/ESCAPE ESCAPE data (2022). ERA5 reanalysis data are obtained from https://cds.climate.copernicus.eu/datasets/reanalysis-era5-single-levels-timeseries?tab=overview (Copernicus Climate Change Service, 2025). UIOOPS software is available at https://doi.org/10.5281/zenodo.1285969 (McFarquhar et al., 2018).

Acknowledgments

We thank all the participants of the campaign, who worked long hours under high uncertainty, enduring challenging circumstances during the COVID-19 pandemic to diligently collect ESCAPE data. We thank the National Science Foundation for their major support of ESCAPE. The authors would like to acknowledge the NSF Grants AGS-2019968, AGS- 2019965, and AGS-2019932. In addition, we would like to acknowledge the support of U.S. DOE Office of Science Biological and Environmental Research Atmospheric System Research (ASR) program (award DE-SC0024317, contract DE-SC0012704, DE-SC0021247 and DE-SC0021160 (SV)) and the Atmospheric Radiation Measurement (ARM) research facility for facilitating and hosting the CSAPR2 deployment at the AMF1. The authors thank Paul Lawson, Qixu Mo and Roelof Bruintjes for processing and sharing the ESCAPE SPEC Learjet data. Furthermore, the authors thank Jeff Snyder for recommending a method for de-aliasing airborne radar Doppler velocities. The authors appreciate the work of the Radar Operations Center, Larry Hopper Jr. of NSSL, and NWSFO Houston personnel (including Rich Businger, Lance Wood, and colleagues) to facilitate Level 1 (time series) data collection with the KHGX radar as part of ESCAPE and TRACER. The computing for this work was primarily performed at the OU Supercomputing Center for Education & Research (OSCER) at the University of Oklahoma (OU).

References

Austin, P. H., Baker, M. B., Blyth, A. M., & Jensen, J. B. (1985). Small scale variability in warm Continental cumulus clouds. *Journal of the Atmospheric Sciences*, *42*(11), 1123–1138. https://doi.org/10.1175/1520-0469(1985)042<1123:ssviwc>2.0.co;2

Baumgardner, D., Abel, S. J., Axisa, D., Cotton, R., Crosier, J., Field, P., et al. (2017). Cloud ice properties: In situ measurement challenges. *Meteorological Monographs*, *58*(9), 1–9.23. https://doi.org/10.1175/AMSMONOGRAPHS-D-16-0011.1

Copernicus Climate Change Service. (2025). ERA5 hourly time-series data on single levels from 1940 to present [Dataset]. *Copernicus Climate Change Service (C3S) Climate Data Store (CDS)*. Retrieved from https://cds.climate.copernicus.eu/datasets/reanalysis-era5-single-levels-timeseries

Cotton, W. R., & Walko, R. (2021). Examination of aerosol-induced convective invigoration using idealized simulations. *Journal of the Atmospheric Sciences*, *78*(1), 287–298. https://doi.org/10.1175/JAS-D-20-0023.1

Ditas, F., Shaw, R. A., Siebert, H., Simmel, M., Wehner, B., & Wiedensohler, A. (2012). Aerosols-cloud microphysics-thermodynamics-turbulence: Evaluating supersaturation in a marine stratocumulus cloud. *Atmospheric Chemistry and Physics*, *12*(5), 2459–2468. https://doi.org/10.5194/acp-12-2459-2012

Dzambo, A. M., Bruning, E., Oue, M., Brunner, K., Singewald, D., Rosky, E., et al. (2025). Forecasting for ESCAPE: A multi-institution hybrid forecasting and nowcasting operation for sea-breeze convection supporting a ground-based and airborne field campaign. *Bulletin of the American Meteorological Society*, *106*(3), E456–E472. https://doi.org/10.1175/bams-d-23-0015.1

Efron, B., & Tibshirani, R. J. (1994). *An introduction to the bootstrap* (1st ed.), Chapman and Hall/CRC. https://doi.org/10.1201/9780429246593

ESCAPE data. (2022). Experiment of sea breeze convection, aerosols, precipitation, and environment [Dataset]. *National Center for Atmospheric Research (NCAR) Earth Observing Laboratory (EOL)*. Retrieved from https://data.eol.ucar.edu/project/ESCAPE

Fan, J., Rosenfeld, D., Zhang, Y., Giangrande, S. E., Li, Z., Machado, L. A. T., et al. (2018). Substantial convection and precipitation enhancements by ultrafine aerosol particles. *Science*, *359*(6374), 411–418. https://doi.org/10.1126/science.aan8461

Fan, J., Zhang, R., Li, G., & Tao, W.-K. (2007). Effects of aerosols and relative humidity on cumulus clouds. *Journal of Geophysical Research*, *112*(D14), D14204. https://doi.org/10.1029/2006jd008136

Fan, J., Zhang, Y., Li, Z., Yan, H., Prabhakaran, T., Rosenfeld, D., & Khain, A. (2025). Unveiling aerosol impacts on deep convective clouds: Scientific concept, modeling, observational analysis, and future direction. *Journal of Geophysical Research: Atmospheres*, *130*(15), e2024JD041931. https://doi.org/10.1029/2024JD041931

Fujiwara, M., Shiotani, M., Hasebe, F., Vomel, H., Oltmans, S. J., Ruppert, P. W., et al. (2003). Performance of the Meteolabor "Snow White" chilled-mirror hygrometer in the tropical troposphere: Comparisons with the Vaisala RS80 A/H-Humicap sensors. *Journal of Atmospheric and Oceanic Technology*, *20*(11), 1534–1542. https://doi.org/10.1175/1520-0426(2003)020<1534:potmsw>2.0.co;2

Grabowski, W. W., & Morrison, H. (2020). Do ultrafine cloud condensation nuclei invigorate deep convection? *Journal of the Atmospheric Sciences*, *77*(7), 2567–2583. https://doi.org/10.1175/JAS-D-20-0012.1

Harris, C. R., Millman, K. J., Van Der Walt, S. J., Gommers, R., Virtanen, P., Cournapeau, D., et al. (2020). Array programming with NumPy. *Nature*, *585*(7825), 357–362. https://doi.org/10.1038/s41586-020-2649-2

Howell, W. E. (1949). The growth of cloud drops in uniformly cooled air. *Journal of Meteorology*, *6*(2), 134–148. https://doi.org/10.1175/1520-0469(1949)006<0134:TGOCDI>2.0.CO;2

Huang, Y., McFarquhar, G. M., Patil, S. U., Gao, L., Taszarek, M., Xue, M., et al. (2025). Dependence of convective cloud microphysical properties on environmental conditions during the TRACER and ESCAPE field campaigns: A synergistic approach of observations, machine learning and parcel models. *Journal of the Atmospheric Sciences*, *82*(10), 2291–2312. in press. https://doi.org/10.1175/JAS-D-24-0269.1

Igel, A. L., & van den Heever, S. C. (2021). Invigoration or enervation of convective clouds by aerosols? *Geophysical Research Letters*, *48*(16), e2021GL093804. https://doi.org/10.1029/2021GL093804

Jensen, M. P., Flynn, J. H., Gonzalez-Cruz, J. E., Judd, L. M., Kollias, P., Kuang, C., et al. (2025). Studying aerosol, clouds, and air quality in the coastal urban environment of southeastern Texas. *Bulletin of the American Meteorological Society*, BAMS-D-23-0331.1. https://doi.org/10.1175/bams-d-23-0331.1

Jorgensen, D. P., Zipser, E. J., & LeMone, M. A. (1985). Vertical motions in intense hurricanes. *Journal of the Atmospheric Sciences*, *42*(8), 839–856. https://doi.org/10.1175/1520-0469(1985)042<0839:vmiih>2.0.co;2

Kollias, P., McFarquhar, G. M., Bruning, E., DeMott, E. J., Kumjian, M. R., Paul Lawson, P., et al. (2025). Experiment of sea breeze convection, aerosols, precipitation, and environment (ESCAPE). *Bulletin America Meteorology Social*, *106*(2), E310–E332. https://doi.org/10.1175/BAMS-D-23-0014.1

Koren, I., Dagan, G., & Altaratz, O. (2014). From aerosol-limited to invigoration of warm convective clouds. *Science*, *344*(6188), 1143–1146. https://doi.org/10.1126/science.1252595

Koren, I., Feingold, G., & Remer, L. A. (2010). The invigoration of deep convective clouds over the Atlantic: Aerosol effect, meteorology or retrieval artifact? *Atmospheric Chemistry and Physics*, *10*(18), 8855–8872. https://doi.org/10.5194/acp-10-8855-2010

Korolev, A. V., & Mazin, I. P. (2003). Supersaturation of water vapor in clouds. *Journal of the Atmospheric Sciences*, *60*(24), 2957–2974. https://doi.org/10.1175/1520-0469(2003)060<2957:SOWVIC>2.0.CO;2

Korolev, A. V., Strapp, J. W., Isaac, G. A., & Nevzorov, A. N. (1998). The Nevzorov airborne hot-wire LWC–TWC probe: Principle of operation and performance characteristics. *Journal of Atmospheric and Oceanic Technology*, *15*(6), 1495–1510. https://doi.org/10.1175/1520-0426(1998)015<1495:TNAHWL>2.0.CO;2

Lebo, Z. (2018). A numerical investigation of the potential effects of aerosol-induced warming and updraft width and slope on updraft intensity in deep convective clouds. *Journal of the Atmospheric Sciences*, *75*(2), 535–554. https://doi.org/10.1175/JAS-D-16-0368.1

LeMone, M. A., & Zipser, E. J. (1980). Cumulonimbus vertical velocity events in GATE. Part I: Diameter, intensity and mass flux. *Journal of the Atmospheric Sciences*, *37*(11), 2444–2457. https://doi.org/10.1175/1520-0469(1980)037<2444:cvveig>2.0.co;2

Lucas, C., Zipser, E. J., & LeMone, M. A. (1994). Vertical velocity in oceanic convection off tropical Australia. *Journal of the Atmospheric Sciences*, *51*(21), 3183–3193. https://doi.org/10.1175/1520-0469(1994)051<3183:vvioco>2.0.co;2

Mascio, J., McFarquhar, G. M., Hsieh, T. L., Freer, M., Dooley, A., & Heymsfield, A. J. (2020). The use of gamma distributions to quantify the dependence of cloud particle size distributions in hurricanes on cloud and environmental conditions. *The Quarterly Journal of the Royal Meteorological Society*, *146*(730), 2116–2137. https://doi.org/10.1002/qj.3782

McFarquhar, G. M., Baumgardner, D., Bansemer, A., Abel, S. J., Crosier, J., French, J., et al. (2017). Processing of ice cloud in situ data collected by bulk water, scattering, and imaging probes: Fundamentals, uncertainties, and efforts toward consistency. *Meteorological Monographs*, *58*, 11.1–11.33. https://doi.org/10.1175/AMSMONOGRAPHS-D-16-0007.1

McFarquhar, G. M., Finlon, J. A., Stechman, D. M., Wu, W., Jackson, R. C., & Freer, M. (2018). University of Illinois/Oklahoma optical array probe (OAP) processing software, version 3.1.4. *Zenodo*. https://doi.org/10.5281/zenodo.1285969

McFarquhar, G. M., & Heymsfield, A. J. (2001). Parameterizations of INDOEX microphysical measurements and calculations of cloud susceptibility: Applications for climate studies. *Journal of Geophysical Research*, *106*(D22), 28675–28698. https://doi.org/10.1029/2000JD900777

Mordy, W. (1959). Computations of the growth by condensation of a population of cloud droplets. *Tellus*, *11*(1), 16–44. https://doi.org/10.3402/tellusa.v11i1.9283

NRC. (2025). NRC flight research laboratory Convair-580 aircraft. Retrieved from https://navigator.innovation.ca/en/facility/national-research-council-canada/nrc-flight-research-laboratory-convair-580-aircraft

Paluch, I. R., & Knight, C. A. (1984). Mixing and the evolution of cloud droplet size spectra in a vigorous continental cumulus. *Journal of the Atmospheric Sciences*, *41*(11), 1801–1815. https://doi.org/10.1175/1520-0469(1984)041<1801:mateoc>2.0.co;2

Patnaude, R. J., McCluskey, C. S., Roberts, G. C., DeMott, P. J., Hill, T. C. J., McFarquhar, G. M., et al. (2025). Characteristics of ice nucleating particles from the long-range transport of Saharan dust. *Geophysical Research Letters*, *52*(11), e2024GL113365. https://doi.org/10.1029/2024GL113365

Pedregosa, F., Varoquaux, G., Gramfort, A., Michel, V., Thirion, B., Grisel, O., et al. (2011). Scikit-learn: Machine learning in python. *Journal of Machine Learning Research*, *12*, 2825–2830.

Politovich, M. K., & Cooper, W. A. (1988). Variability of the supersaturation in cumulus clouds. *Journal of the Atmospheric Sciences*, *45*(11), 1651–1664. https://doi.org/10.1175/1520-0469(1988)045,1651:VOTSIC.2.0.CO;2

Prabha, T. V., Khain, A., Maheshkumar, R. S., Pandithurai, G., Kulkarni, J. R., Konwar, M., & Goswami, B. N. (2011). Microphysics of premonsoon and monsoon clouds as seen from in situ measurements during the cloud aerosol interaction and precipitation enhancement experiment (CAIPEEX). *Journal of the Atmospheric Sciences*, *68*(9), 1882–1901. https://doi.org/10.1175/2011JAS3707.1

Proakis, J. G., & Manolakis, D. G. (2021). *Digital signal processing* (5th ed.). Pearson Education.

Pruppacher, H. R., & Klett, J. D. (1978). *Microphysics of clouds and precipitation*. Springer Netherlands. https://doi.org/10.1007/978-94-009-9905-3

Roberts, G., Ranjbar, K., Nichman, L., Wolde, M., McCluskey, C., Takeishi, A., et al. (2026). Marine aerosol to refinery emissions: Transport and evolution of CCN in the Houston Metropolitan area and their impact on cloud formation. *Journal of Geophysical Research: Atmospheres*. https://doi.org/10.1029/2025JD044628

Romps, D. M. (2017). Exact expression for the lifting condensation level. *Journal of the Atmospheric Sciences*, *74*(12), 3891–3900. https://doi.org/10.1175/JAS-D-17-0102.1

Romps, D. M. (2025). A method for calculating reliable supersaturation reveals low values in tropical rainy-season clouds. *Journal of the Atmospheric Sciences*, *82*(8), 1517–1527. https://doi.org/10.1175/JAS-D-24-0265.1

Romps, D. M., Latimer, K., Zhu, Q., Jurkat-Witschas, T., Mahnke, C., Prabhakaran, T., et al. (2023). Air pollution unable to intensify storms via warm-phase invigoration. *Geophysical Research Letters*, *50*(2), e2022GL100409. https://doi.org/10.1029/2022GL100409

Sheffield, A. M., Saleeby, S. M., & Van Den Heever, S. C. (2015). Aerosol-induced mechanisms for cumulus congestus growth. *Journal of Geophysical Research: Atmospheres*, *120*(17), 8941–8952. https://doi.org/10.1002/2015JD023743

Shen, C., Zhao, C., Ma, N., Tao, J., Zhao, G., Yu, Y., & Kuang, Y. (2018). Method to estimate water vapor supersaturation in the ambient activation process using aerosol and droplet measurement data. *Journal of Geophysical Research: Atmospheres*, *123*(18), 10–606. https://doi.org/10.1029/2018jd028315

Squires, P. (1952). The growth of cloud drops by condensation. I. General characteristics. *Australian Journal of Chemistry*, *5*(1), 59–86. https://doi.org/10.1071/ch9520059

Stein, A. F., Draxler, R. R., Rolph, G. D., Stunder, B. J. B., Cohen, M. D., & Ngan, F. (2015). NOAA's HYSPLIT atmospheric transport and dispersion modeling system. *Bulletin of the American Meteorological Society*, *96*(12), 2059–2077. https://doi.org/10.1175/BAMS-D-14-00110.1

Varble, A. (2018). Erroneous attribution of deep convective invigoration to aerosol concentration. *Journal of the Atmospheric Sciences*, *75*(4), 1351–1368. https://doi.org/10.1175/JAS-D-17-0217.1

Varble, A. C., Igel, A. L., Morrison, H., Grabowski, W. W., & Lebo, Z. J. (2023). Opinion: A critical evaluation of the evidence for aerosol invigoration of deep convection. *Atmospheric Chemistry and Physics*, *23*(21), 13791–13808. https://doi.org/10.5194/acp-23-13791-2023

Virtanen, P., Gommers, R., Oliphant, T. E., Haberland, M., Reddy, T., Cournapeau, D., et al. (2020). SciPy 1.0: Fundamental algorithms for scientific computing in Python. *Nature Methods*, *17*(3), 261–272. https://doi.org/10.1038/s41592-019-0686-2

Warner, J. (1968). The supersaturation in natural clouds. *Journal de Recherches Atmospheriques*, *3*(3), 233–237.

Yeom, J. M., Yum, S. S., Mei, F., Schmid, B., Comstock, J., Machado, L. A. T., & Cecchini, M. A. (2019). Impact of secondary droplet activation on the contrasting cloud microphysical relationships during the wet and dry seasons in the Amazon. *Atmospheric Research*, *230*, 104–648. https://doi.org/10.1016/j.atmosres.2019.104648